Electrochimica Acta 383 (2021) 138348

Contents lists available at ScienceDirect

Electrochimica Acta

journal homepage: www.elsevier.com/locate/electacta

Effect of the residual silver and adsorbed lead anions towards the electrocatalytic methanol oxidation on nanoporous gold in alkaline media ☆

Alex Ricardo Silva Olaya [a], Birthe Zandersons [b], Gunther Wittstock [a,*]

[a] School of Mathematics and Science, Department of Chemistry, Carl von Ossietzky University of Oldenburg, 26111 Oldenburg, Germany
[b] Institute of Materials Physics and Technology, Hamburg University of Technology, Hamburg 21073, Germany

ARTICLE INFO

Article history:
Received 29 December 2020
Accepted 2 April 2021
Available online 9 April 2021

Keywords:
Nanoporous gold
Methanol oxidation
Under potential deposition
Electrocatalysis
Surface structure

ABSTRACT

Nanoporous gold (NPG) obtained by potentiostatic dealloying of an AuAg master alloy was pulverized, filled into a cavity microelectrode and its surface electrochemistry was investigated in NaOH and KOH solutions. This method yielded highly resolved undistorted voltammograms of this polycrystalline material with clear evidences for surface segregation of Ag during storage in air. One cycle in 0.1 M H_2SO_4 can remove most of the residual Ag from the surface as evidenced by voltammetry after back transfer to alkaline solution and by X-ray photoelectron spectroscopy (XPS). After removal of residual Ag from the surface, the surface undergoes rephasing forming wider {111} and {110} terraces as evidenced by Pb underpotential deposition (UPD). By adjustment of the bulk concentration of Pb^{II} species, a selective partial coverage of the high internal surface area of NPG could be intentionally adjusted. Lead species remain attached to the NPG surface at potentials positive of the UPD regions either as plumbates or Pb^{IV} species as evidenced by XPS. Those tools enable to disentangle effects on the electrocatalysis of the methanol oxidation reaction (MOR) in different potential regions for 1 M methanol in different concentrations of NaOH and KOH. The MOR commences at lower potentials in the presence of residual Ag. At very high potential, the presence of Ag species promotes the oxidation to CO_2/CO_3^{2-}. Tafel analysis after selective blocking of specific facets shows that the {110} terraces promote especially the first step of MOR while the {111} terraces enhance the rate of further steps that are rate-limiting at higher potentials. While high coverages by Pb UPD layers or adsorbed plumbate anions inhibit electrooxidation, the behavior of NPG electrodes with low coverages of Pb species is reminiscent to NPG electrodes with residual Ag. This could be caused by promoting the methoxide and/or OH^- adsorption at low overpotentials and catalyzing complete oxidation by a surface bound Pb^{IV} species at higher potentials. The catalytic currents increase with base concentration and are higher for KOH compared to NaOH. Comparable effects of base concentration on the parameters of the Tafel lines suggest that this effect is a result of slightly stronger deprotonation of methanol in bulk KOH solutions.

1. Introduction

Nanoporous gold (NPG) consists of nanometer-sized struts (called 'ligaments') and interconnected pores in a similar size regime. This material has gained attention as porous noble metal electrode material in application requiring high surface area, chemical inertness as well as electrical and thermal conductivity such as sensors [1–3], supercapacitors [4,5], actuators [6,7], and electrocatalyst [8,9]. It is also regarded as an interesting model system for exploring approaches for the rational design of electrocatalysts [10] because of the possibility to compare the electrocatalytic behavior to corresponding reaction in the gas phase [11] or catalytic action in chemical partial oxidation in liquid phase [12]. Furthermore, important features such as the ligament size [13], structure [14] and elemental composition [15,16] can be systematically tuned in order to study the resulting effects on (electro)catalytic reactions [10].

☆ Manuscript prepared for Electrochimica Acta Special Issue for Belgrade online.

* Corresponding author.
E-mail addresses: alex.r.silva@uni-oldenburg.de (A.R. Silva Olaya), birthe.zandersons@tuhh.de (B. Zandersons), wittstock@uol.de, gunther.wittstock@uni-oldenburg.de (G. Wittstock).

https://doi.org/10.1016/j.electacta.2021.138348

There are different approaches to obtain NPG. Gold can be electrodeposited in voids of nanoscale templates [17] or obtained by potential cycling Au electrodes in $ZnCl_2$/benzyl alcohol electrolyte [8]. Arguably, the most popular approach is based on electrochemically dissolving (leaching) the less noble element from a binary gold-containing alloy [18,19], a process named dealloying. This process yields macroscopic monoliths in the shape of the starting material. Attractive starting materials, also called master alloys, are silver-rich alloys (Ag_xAu_{1-x} with the Ag mole fraction x larger than the parting limit measured as 0.6 [20]) because Ag and Au have nearly the same atomic size and form a stable solid solution over the entire concentration range [21]. Master alloys with Cu [22] Al [23,24], Ni [25], and Zn [26] have also been investigated. The dealloying process must be controlled in order to balance the rates of oxidative removal of Ag atoms with the surface diffusion of the remaining Au atoms that cause the formation and defined growth of pores and ligaments [27]. This has been achieved by corrosion in concentrated nitric acid (called free corrosion, FC) [28], potential-controlled electrolytic dissolution (PCD) as also used in this work [20,29,30] or current-controlled dissolution (GCD) [16] in aqueous solutions of H_2SO_4 or $HClO_4$.

Because of thermodynamic reasons, NPG obtained by dealloying Ag_xAu_{1-x} always contains a residual Ag content. However, the residual Ag contents with typical Ag mol fraction x_{Ag} are between 0.5 and 10 % [16,31] and thus much higher than predicted by thermodynamics [16,32–34]. As Ag can dissolve only from the alloy|solution interface in the dealloying process, the residual content of the less noble metal is controlled by the time available for surface diffusion that uncovers buried Ag atoms and make them accessible for solution. At the same time, surface diffusion leads to a state of lower surface energy that results in larger ligaments and pores. This process, called coarsening, occurs concomitantly with the diminution of the residual Ag content [31,35]. For instance, potentiodynamic dealloying tends to yield a material with a ligament size of ca. 45 nm [36,37]. The residual Ag atoms are not necessarily randomly distributed within single ligaments but Au layers may cover regions that have essentially the composition of the master alloy [32,35].

After completion of the dealloying process, the total Ag content in NPG remains constant because a release of Ag^+ into the liquid phase is not possible. However, the distribution of Ag atoms within the ligaments may change by surface segregation promoted by surface oxidation even by storage in air. The details and the extend of this process are not clear yet. DFT and Monte Carlo simulations showed that the presence of oxygen adsorbed on the surface promotes the Ag segregation, while a clean surface exposed to vacuum causes gold enrichment [38]. Fujita et al. [39,40] determined a high density of low coordinated steps and kinks on the NPG surface by TEM. They proposed that residual Ag is located in these places stabilizing the high energy surface structure and blocking the thermodynamically expected {111} faceting of Au. Later, the theoretical study of Moskaleva et al. [41] supported this hypothesis. Previous work from this laboratory using photoelectron spectroscopy has shown that Ag segregation occurs even in vacuum at around 100°C concomitantly with the decomposition of Ag(I) species and the removal of ubiquitous organic contaminants [42]. An enrichment of Ag at the surface was also found after electrochemical treatment of the samples. This process was accompanied by strong coarsening. The enrichment factor of surface to bulk Ag mole faction $x_{Ag,surf}/x_{Ag}$ increased with decreasing overall Ag content [42].

The formation and reduction of surface oxides by potential scans tends to promote surface restructuring of the NPG ligaments to wider terraces of low-index facets, where the preference for {111} or {100} can be tuned by the specific potential program [14]. This restructuring can be prevented if Ag(I) species are not dissolved from the surface in alkaline solution [43]. Interestingly, a single potential scan in acidic electrolyte is sufficient to lift the blockade of the surface restructuring. This is in agreement with the notion, that Ag species hinder surface diffusion at high energy surface sites [43]. This observation was enabled by the use of cavity microelectrodes that allow the recording of well-resolved surface voltammetry with minimized disturbance of uncompensated resistance and mass transport limitations [43].

There are contradictory reports on the coarsening of NPG during electrocatalytic reactions that are apparently linked to details of the dealloying and post-dealloying modification. While Ju et al. [8] reported about NPG structure that proved stability even after 100 potential cycles of methanol oxidation reaction (MOR), Zhang et al. [9] found that NPG obtained by free corrosion tends to coarsen during prolonged MOR. A low content of Pt on the surface of the ligaments, either as a result of dealloying a ternary AgAuPt alloy [44] or obtained by deposition of Pt on NPG [9] stabilizes the ligaments against coarsening caused by surface diffusion of Au.

The objective of this study is to probe the development of specific facets using the signatures of underpotential deposition (UPD) and the corresponding oxidation processes to study the effect of such facets for the electrocatalytic performance of NPG in alkaline media. We also discovered that the use of NPG in cavity microelectrodes allows to adjust well-defined partial UPD coverages that can be used to selectively shut-off electrocatalytic reaction of specific sites. This adds an interesting new possibility to study structure-reactivity relationships on complex electrode materials. Lead UPD on gold has shown to be very sensitive to the different surface structures in acidic electrolytes [45,46]. Varying systematically the gold surface, Hamelin explored the effects of steps and kinks on the surface voltammetry [45]. In absence of specifically adsorbed anions, the UPD results for those sites followed the trend found in ultra-high vacuum (UHV) studies irrespective of the presence of water as competing adsorbate in the electrochemical cell only [46]. Pb UPD has been applied broadly as an analytical tool for surface structures on Au mostly in acidic electrolytes. The increasing interest for electrocatalysis in alkaline media has also prompted the application of Pb UPD for the characterization of the surface structure of Au nanoparticles in alkaline media, where well-defined peaks were identified at different potentials for each basal plane [47]. This is enabled by the formation of soluble plumbites $[Pb^{(II)}(OH)_m]^{(m-2)-}$ in alkaline solutions. Additionally, Pb ions can form PbO_2 below the potential of gold surface oxidation [48]. The oxidizing nature of PbO_2 was reported to remove organic surface contamination and to protect the surface from restructuring [47]. We use the methanol oxidation reaction (MOR) in alkaline media as a test reaction, for which NPG shows a higher reactivity than flat Au electrodes [8,9,49]. The role of residual Ag for the electrocatalysis of partial methanol oxidation is not entirely clear. For CO oxidation in the gas phase catalysis, it is known that a small amount of residual Ag in NPG promotes the dissociation of molecular oxygen and thus CO oxidation, while a large amount of Ag is disadvantageous [40]. A similar reasoning seems to apply for MOR with an additional effect on product distribution, especially the formation of methyl formate [11,12]. Our previous study on electrocatalytic MOR showed that the binding state of residual Ag as characterized by X-ray photoelectron spectroscopy (XPS) changes during MOR without clear indication on its mechanistic role [49].

2. Experimental section

2.1. Reagents

Sulfuric acid, (96%, Suprapur®, Merck, Darmstadt, Germany), hydrochloric acid (Suprapur®, Merck), potassium hydroxide hydrate (99.995%, Suprapur®, Merck), sodium hydroxide hydrate

(99.995%, Suprapur®, Merck), potassium nitrate (99.995%, Suprapur®, Merck), lead(II) nitrate (99.999%, trace metal basis, Merck), Pb (99.95%, trace metal basis, Merck), PbO (99.999%, trace metal basis, Merck), PbO_2 (99.998%, trace metal basis, Merck), perchloric acid (70% Emsure, Merck) and methanol (Uvasol®, Merck) were used as received. Solutions were made with ultrapure water (0.05 μS cm^{-1}), in all cases the volume used is 20 mL. Argon 99.999% (Alphagaz^{TM}, Airliquide, Düsseldorf, Germany) is bubbled for at least 20 min prior to each experiment, and the Ar flow is kept in the head space during the measurement in order to maintain the inert atmosphere.

2.2. NPG samples

Nanoporous gold samples were obtained by potentiodynamic dealloying of an $Ag_{75}Au_{25}$ master alloy as detailed in Ref. [43]. In short, Ag and Au wires (Ag 99.99%, Au 99.99%, Sigma-Aldrich) are alloyed by arc melting in Ar atmosphere (MAM-1 E. Bühler), homogenized in an evacuated quartz tube for 5 days at 850 °C (10^{-2} bar, RHF1600, Carbolite), drawn to a diameter of 0.95 mm and cut into cylinders of 1.9 mm length. Mechanical defects introduced by the mechanical treatment were healed by annealing the samples in an evacuated furnace at 650 °C for 3 h (Mila-5000, Ulvac-Rico). For dealloying, an $Ag_{75}Au_{25}$ cylinder was mounted as working electrode in a three-electrode cell completed by a Ag wire as auxiliary electrode and a Ag/AgCl as reference electrode connected to an potentiostat (PGSTAT, Autolab-Metrohm). The sample was oxidized at 1.25 V vs. SHE in 1 M $HClO_4$ until the current dropped to 15 μA. Then, the potential was incremented to 1.35 V and held until the current had decayed to 15 µA. Subsequently, the sample was cleaned by 20 potentiodynamic cycles between 0.1 V and 1.6 V in fresh 1 M $HClO_4$ at 5 mV s^{-1} followed by keeping the potential at 1.35 V for 20 min. Finally, the sample was cycled 20 times at 5 mV s^{-1} between 0.1 V and 1.6 V in fresh 1 M $HClO_4$ ending at 0.8 V. Afterwards, the sample was rinsed in ultrapure water and dried in air for 1–2 days and stored in closed containers under air for further use. The NPG samples are characterized by an average ligament diameter of 40 nm, a specific surface area of 11.8 m^2 g^{-1}, and a density of 4.99 g cm^{-3}. The residual Ag mole fraction x_{Ag} was determined as 1% by EDX.

The NPG powder was obtained from the monolith by first sonicated it in a clean vial for 5 min followed by triturating in an agate mortar until no appreciable changes in the grain size were observable. The material thus obtained is called here *"as-prepared"*. The powder was used for a period of 6 month after preparation. For referencing, a sample with reduced amount of residual Ag at the surface of the ligaments was prepared by filling a fraction of the NPG powder into a cavity microelectrode and cycling it 3 times between -0.649 V and +0.941 V vs. $Hg/HgSO_4/K_2SO_{4(sat)}$ in 0.1 M H_2SO_4 followed by and rinsing with ultrapure water. For brevity, this sample is called *"after cycling in H_2SO_4"*.

2.3. Electrochemical characterization

Cavity microelectrodes (CME) were produced by sealing a 1.5 cm gold wire of 100 µm diameter (99.99+%, Goodfellow, Friedberg, Germany) in a borosilicate glass capillary which was previously heated to form a tip. The assembly was grinded with grade 1500 abrasive paper to expose the disk-shape cross-section of the Au wire followed by polishing with abrasive papers of 15, 9, 3, and 1 μm grain size. Finally, this disk-shape cross section tip is polished to mirror finish using an microgrinder (EG-401, Narishige, Tokyo, Japan). Subsequently, the Au wire inside the capillary was connected to a Cu wire with silver-epoxy glue (EPO-TEKs, John P. Kummer GmbH, Germany).

The cavities were formed by potentiostatic dissolution of the exposed gold at +1.1 V vs. a saturated calomel electrode (SCE, from ALS, Tokyo, Japan) in 1 M HCl [50] during 60 s and cycling 10 times at 100 mV/s between 0.5 V and 1.5 V vs. SCE. The quality of polishing of the microelectrodes and the depth of the cavities [(21 ± 1) µm] was verified using a confocal laser scanning microscope (TCS SP2, Leica Microsystems GmbH, Germany) with a HC PL Fluotar 50x/0.8 dry lens. The obtained CME is immersed in piranha solution for 1 h and transferred to ultrapure water for at least 24 h before use. The cavity was filled by slightly pressing the CME into NPG powder. The end of the filled CME was washed with ultrapure water and excess NPG powder outside the cavity was wiped off with a soft cloth. The filling is monitored by inspection with a 6× magnifying lens.

The electrochemical cell is built with a 25 mL glass vial and a Teflon® cap with five necks. A CME filled with the sample was used as working electrode, an Au coil as auxiliary electrode. The reference electrodes were $Hg/HgSO_4/K_2SO_{4(Sat)}$ (from ALS,) in Cl^--free acid media and a Hg/HgO/1 M NaOH (from ALS) in alkaline media, to which the potential is referred in the description of UPD and electrocatalytic experiments. Electrochemical characterization was performed on a potentiostat with an analog scan generator (PGSTAT128N, Autolab-Metrohm, Filderstadt, Germany with scan250 and NOVA 2.1 software).

All glassware was cleaned by immersion in 1 g/L $KMnO_4$ solution acidified with 20 mL/L solution of 96 % (m/m) H_2SO_4 for at least 24 h. Next, it was immersed in 40 mL/L 30 % H_2O_2 solution acidified with 20 mL/L solution of 96 % (m/m) H_2SO_4 until there is no visual evidence of purple color. *Caution: This mixture colloquially known 'Piranha solution' reacts violently with all organic materials. The solution has to be handled with extreme care to avoid personnel injury and property damage.* Finally, it was rinsed with ultrapure water and boiled three times.

Alkaline lead-containing solution was prepared dissolving the KOH and KNO_3 in half of the final volume, after which $Pb(NO_3)_2$ was added. This order is important to avoid the oxidation of Pb^{2+} to Pb^{4+} promoted by the dissolved oxygen in highly alkaline medium.

2.4. Structural and compositional characterization

The characterization of the porous structure as well as the grain size of the NPG powder were performed with a scanning electron microscope (Helios Nanolab 600i system, FEI Company) equipped with an EDX detector using an acceleration voltage of 15 kV and a working distance of around 4 mm. The surface composition of NPG ligaments was characterized by XPS (ESCALAB 250Xi, Thermo Fisher Scientific, East Grinstead, UK) working with a monochromatized Al Kα source. The survey spectra were taken with a pass energy of 100 eV (energy step size of 1 eV) while a pass energy of 10 eV (energy step size 0.02 eV) was used for high resolution spectra. Powders of Pb, PbO and PbO_2 were compressed in a homemade brass sample holder with a cavity of 5 mm diameter and 2 mm depth using a pressing tool. The measurement could be performed without charge compensation. Using charge compensation on those samples lead to differential charging. The lead metal reference sample was Ar^+-sputtered for 60 s until signals of O and C passive and contamination layers disappeared.

3. Results and discussion

3.1. Morphological and electrochemical characterization of NPG samples

Figure 1A shows the scanning electron microscopy (SEM) images of NPG powder samples after filling them into the CME. Liga-

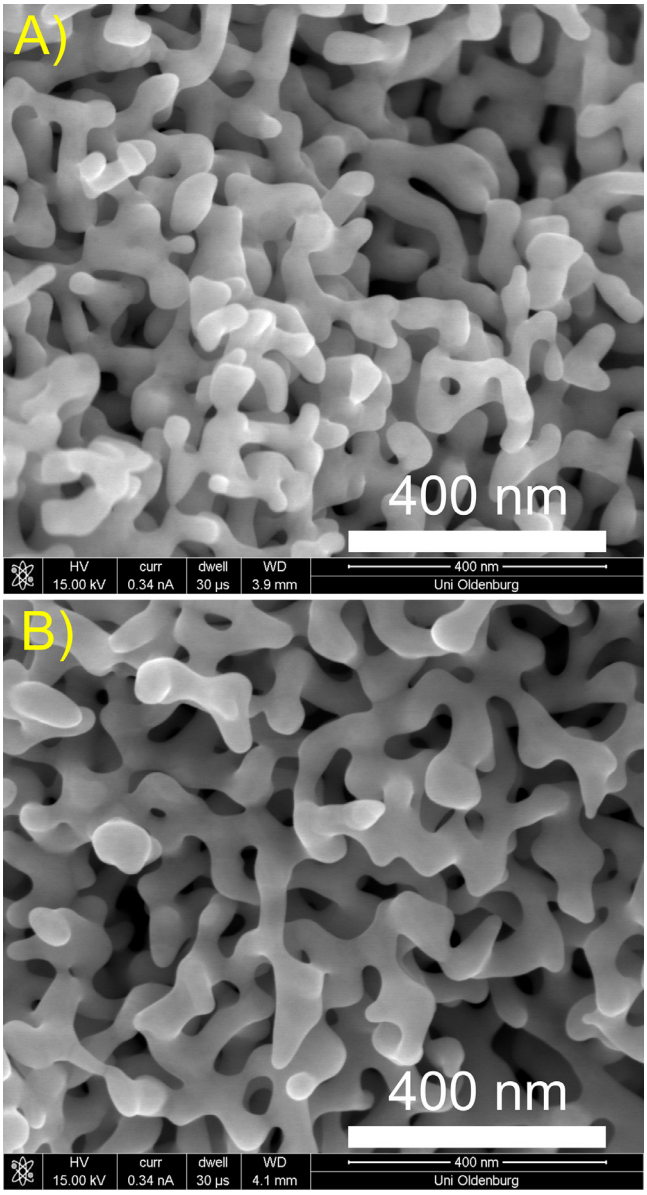

Fig. 1. SEM images of nanoporous gold after filling in a cavity microelectrode; (A) *"as prepared"* and (B) *"after cycling in H_2SO_4"*.

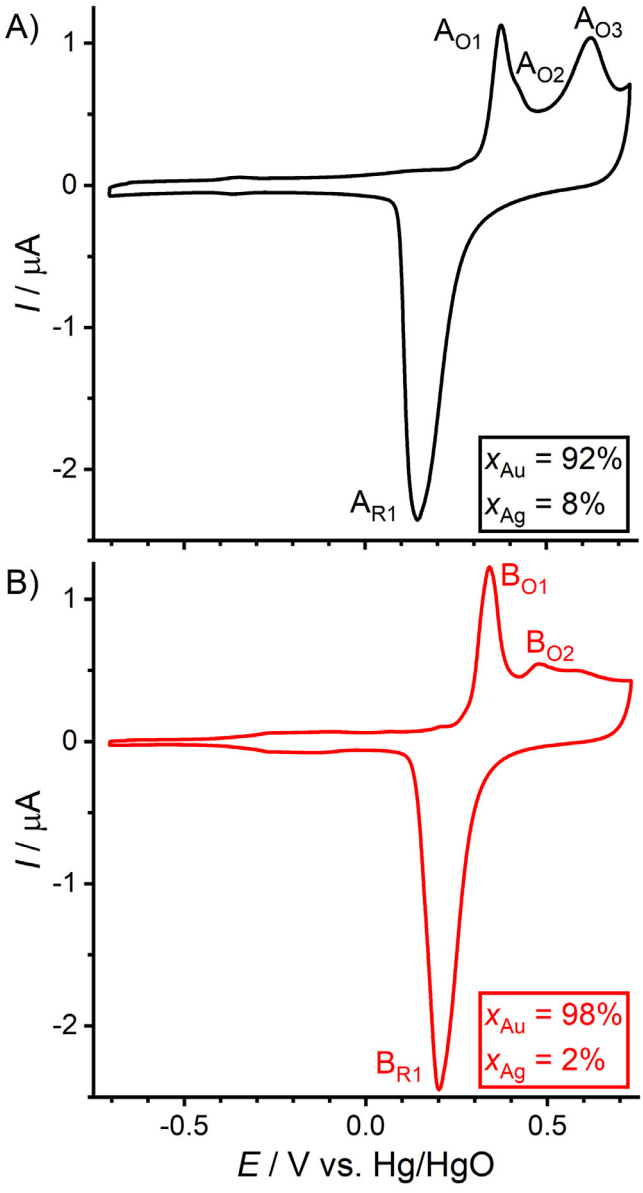

Fig. 2. Voltammogram of (A) *"as prepared"* and (B) *"after cycling in H_2SO_4"* NPG samples in 0.1 M KOH, v = 10 mV s^{-1}. Squares in each color correspond to the atomic proportion of gold and silver determined by XPS.

ments have an average diameter of 40 nm, in agreement with the size reported in previous studies [51–53]. The mesoporous network is not affected by the mechanical forces acting during the powder preparation and filling of the cavity. This is an important first observation because it suggests that the results obtained with pulverized NPG in a CME can be extrapolate to the complete monolith. Moreover, assuming that the new surface created by the pulverization process is negligible compared to the internal surface area of the initial ligament structure, the electrochemical properties of the NPG surface can be extrapolated to the monolith as well.

Figure 1B shows the SEM images of NPG *"after cycling in H_2SO_4"* as detailed in the Experimental section. The morphology is virtually indistinguishable from Fig. 1A, but the porous network seems to be slightly less compact. The average ligament diameter in Fig. 1B is about 40 nm and thus indistinguishable from the feature size of the "*as-prepared*" state in Fig. 1A. These facts evidence that the porous morphology is maintained during the whole preparation process of the two samples.

Figure 2 shows the electrochemical characterization of both NPG samples in 0.1 M KOH. The *"as-prepared"* sample (Fig. 2A) exhibits an almost pure capacitive current below 0.00 V. There is a small current increase followed by a plateau zone between 0.10 V and 0.30 V in the positively going scan that has previously been attributed to the specific adsorption of OH^- on the surface [54]. At potentials positive of 0.3 V, the surface exhibit three oxidation peaks: The signal A_{O1} at 0.38 V with the shoulder A_{O2} at 0.42 V are produced by the gold surface oxidation. As discussed in our previous work [43], A_{O3} at 0.62 V is provoked by the presence of residual Ag at the ligament surface. This peak disappears after short cycling in H_2SO_4 solution (Fig. 2B, vide infra). The presence of Ag species at the surface of NPG stabilizes the high energetic kinks and steps of the ligaments during cycling in alkaline solutions. The asymmetric peak A_{R1} (Fig. 2A) originates from the reduction of the surface oxides and is followed by a fast desorption of OH^- and the capacitive zone in the negatively going scan.

Figure 2B shows the voltammogram of NPG recorded in 0.1 M KOH *"after cycling in H_2SO_4"* and transfer to the alkaline solution. In comparison to Fig. 2A, the potential range of purely capacitive behavior is narrowed (-0.71 V to -0.35 V). In the positively going scan, the current increases and reaches a plateau zone between -0.30 V to 0.25 V with a slight increase positive of 0.19 V suggesting a wider potential range in which the specific hydroxide (OH^-) adsorption takes place than in Fig. 2A. The signals for the surface oxidation in the positively going scan in Fig. 2B exhibit significant differences to Fig. 2A. The oxidation peak B_{O1}, which corresponds to peak A_{O1}, is shifted to lower potential evidencing that this surface is oxidized more easily. Prominent changes are seen at potentials positive of 0.6 V, where no oxidation peak is observed in Fig. 2B, while a large signal was observed for the "*as prepared*" sample in Fig. 2A. This evidences that cycling in H_2SO_4 completely eliminates the surface structures that are involved in the process causing the signal A_{O3}. The short cycling of the sample in H_2SO_4 before back transfer to KOH solution also affects the signals in the natively going scan in Fig. 2B. The peak B_{R1} for the reduction of surface oxides is more symmetrical and shifted to more positive potential indicating that less driven force is required to trigger the reaction.

The peak A_{O3} has been attributed to the oxidation of Ag that remains from the dealloying process in NPG [43]. Furthermore, it has been proven by transmission electron microscopy that NPG often contains regions within individual ligaments with the composition of the master alloy [32,35] in agreement with the notion that those regions had remained shielded from the dealloying processes. These regions constitute a Ag reservoir for equilibration processes. It has been also measured that the Ag mole fraction x_{Ag} in the topmost layers of the ligaments is higher than in the bulk of ligaments [42]. However, during our dealloying process Ag is thoroughly removed from the surface by prolonged polarization in acidic solution at oxidizing potential followed by cycling (see Experimental section). These considerations suggest that this surface Ag excess builds up after the dealloying procedure. We observe peak A_{O3} consistently with peak currents that increase with storage time of NPG in air over the investigated time spans (2 weeks to 6 months). The surface segregation may be promoted by the oxidation of the surface in air as suggested by literature summarized in the Introduction [38–42] To the best of our knowledge, there are no reports about the evolution of NPG surface stored in oxygen-free atmosphere for prolonged times which would allow a comparison to the storage in oxygen-containing atmosphere. There is a second interpretation of the data that deserves consideration: Ag species at the surface stabilizes the highly curved surface structure of ligaments formed during the dealloying process as it has been proposed by theoretical studies [41]. During dealloying, the critical potential [27] shifts to higher values with decreasing Ag content, until the Ag dissolution from the surface ceases. In any case, it is worth to characterize the surface structure of NPG in the "*as prepared*" state and "*after cycling in H_2SO_4*" before back transfer to 1 M KOH. This may help to understand the trend of post-dealloying changes of NPG as well as to rationalize the impact of the surface structure on the electrocatalytic performance of the material.

3.2. Determination of the surface structure by Pb under potential deposition

Pb UPD was used as a diagnostic tool for changes of surface structure and composition on NPG because this UPD process causes separate signals for each facet of an Au surface at very characteristic potentials [55]. Unlike many other UPD processes, Pb UPD also works in alkaline pH [56] because Pb(II) species are soluble in alkaline media as plumbites $[Pb(OH)_m]^{(2-m)-}$ ($m > 2$). Fig. 3 shows the cyclic voltammograms of NPG obtained in Pb(II)–containing alkaline solution in the potential window of Pb UPD.

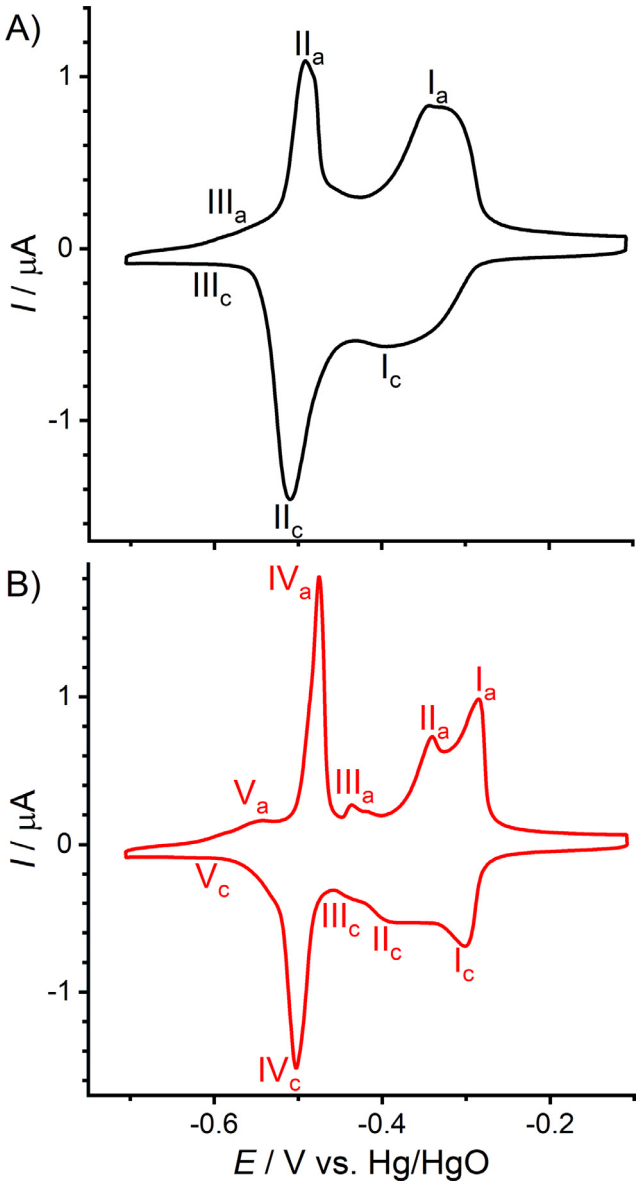

Fig. 3. Voltammogram (5th cycle) of (A) *"as prepared"* and (B) *"after cycling in H_2SO_4"* NPG in 1×10^{-3} M $Pb(NO_3)_2$ + 0.1 M KNO_3 + 0.1 M KOH, v = 10 mV s^{-1}.

Fig. 3A corresponds to the recorded CV of *"as-prepared"* and Fig. 3B to the *"after cycling in H_2SO_4"* sample.

Figure 3A shows a broad peak I_c between -0.29 V and -0.43 V of low intensity in the negatively going scan followed by a more intense peak II_c between -0.45 V and -0.56 V, which decays towards a quasi-plateau zone III_c. The positively going scan shows a peak III_a of low intensity followed by a more intense peak II_a between -0.53 V and -0.46 V, which seems to be composed of two signals. Next, a broad peak I_a emerges between -0.43 V and -0.28 V. Peaks I_c and I_a are related to the Pb deposition and Pb dissolution, respectively, on the {110} domains and defects surrounding these domains [47]. In comparison to peak I_a, the lower current of peak I_c suggests a sluggish deposition process, and a faster dissolution of the layer that has been formed. This behavior is not observed at other highly curved surfaces, such as nanoparticles [47] or nanorods [57], which show similar signals for the deposition/dissolution process of the Pb layer. This difference in the behavior might originate from the presence of Ag on the surface, which obstructs the location of the Pb ion on the gold atoms sur-

rounding it. The couple II_c – II_a corresponds to the deposition and dissolution of Pb on the {111} domains [47]. Because $|I_{p,IIc}|/|I_{p,IIa}|$ is greater than 1, the deposition process is faster than the dissolution on the domains.

The voltammogram of NPG "*after cycling in H_2SO_4*" (Fig. 3B) exhibit much better resolved peaks in the negatively and the positively going scan. The negatively going scan shows the peaks I_c and II_c between -0.27 V and -0.43 V, respectively. A new small peak III_c between -0.43 V and -0.46 V is followed by a narrow peak IV_c between -0.46 V and -0.57 V with a shoulder V_c centered at -0.54 V. The positively going scan shows a low intensity peak V_a followed by a narrow peak IV_a, a small peak III_a with a shoulder between -0.45 V and -0.40 V and two peaks, II_a and I_a, between -0.39 V and -0.26 V. The couple IV_c – IV_a corresponds to the deposition/dissolution of Pb at/from {111} domains [47]. Those domains seem to be surrounded by defects causing the small signals V_c – V_a. In this case, the dissolution of the Pb UPD layer on the {111} facets is 20% faster than the deposition ($|I_{p,IVc}|/|I_{p,IVa}| = 0.8$), which is similar to the behavior of Au(111) single crystal electrodes. This suggests the development of wider {111} domains on the ligaments of NPG. The couple III_c – III_a originates from domains with {100} structure, domains of {110} structure are responsible for the resolved II_c – II_a couple. Finally, the couple I_c – I_a remains as the deposition and dissolution signal of the Pb layer on the high energetic defects of the ligament surface near {110} domains [47].

The conclusions from the change in the Pb UPD signals on NPG in 0.1 M KOH before and after a transfer and cycling in H_2SO_4 are summarized schematically in Fig. 4. After the dealloying process, the surface of the ligaments contains small terraces and a high density of defects such as steps and kinks that allow a highly curved surface (Fig. 4A). Although sluggish coverage of Pb on single crystal Au(110) complicates the interpretation of the peak I_c, the low current that the process shows on NPG is remarkable. This can be explained by having in mind that the surface is made up of a high number of defects nearby small terraces, that curve the surface and even expose circular pores, as represented in Fig. 4A. On this surface the deposition of a compact UPD monolayer is less favorable than on flat Au surfaces because of the decreasing lateral interaction between Pb atoms on concave zones (marked with red circles in Fig. 4A), and the increased repulsion and geometrical hinderance in convex zones (marked with blue circles in Fig. 4A). Additionally, the Pb interaction with Au embedded in zones which are rich in residual Ag must be different because of the electronic influence of the interaction Pb – Ag [58]. This interaction is less favorable than Pb – Au [59] shifting the deposition potential to more negative values [60,61]. This last effect, distributed throughout the whole surface may explain the broader base of the peaks II_c – II_a in Fig. 4A compared to Fig. 4B. They are very narrow in Au(111) facets. Finally, defects near wider terraces are responsible for the peaks III_c – III_a, as depicted in Fig. 4A. Following the reasoning of Hernandez et al. [56] who found that single crystal electrodes do not show peaks below 0.40 V vs RHE (-0.51 V vs. Hg/HgO at pH 13), we conclude that the signals III_a and III_c in Fig. 3A must arise from the edges between two low index facets of the surface of a ligament.

After cycling the sample in H_2SO_4 solution, the Pb UPD voltammogram shows better defined and narrower peaks than the "*as-prepared*" samples. This result reveals that the surface developed wider domains. This occurs concomitantly with the reduction of the Ag mole fraction on the surface of the ligaments as measured by XPS [43]. Those findings are illustrated in Fig. 4B by wider terraces (compared to Fig. 4A) intersected by a much lower step density than in the "*as-prepared*" state. The peaks I_c – I_a in Fig. 4B arise from Pb UPD on those defects, and the couple II_c – II_a arises from the UPD process on well-developed {110} domains. The conversion from the broad peak I_a of Fig. 4A to the two, well resolved peaks I_a and II_a in Fig. 4B is a strong indication for the restructuring of the ligament surface. Because this process only takes place in acidic electrolytes [43], it is plausible that residual Ag is resolved during potential cycling in acidic electrolytes and that is was acting as the stabilizer of the highly curved parts of the ligaments against a structural rearrangement during potential cycling in alkaline electrolytes. This statement is also supported by the development of {100} domains, which give rise to the signals III_c – III_a in Fig. 3B. These signals do not have an equivalent in Fig. 3A. Besides, peaks IV_c – IV_a narrowed in Fig. 3B (≈ 20 mV), which is much closer to the result obtained with Au(111) single crystal electrodes [47], indicating a widening of the {111} domains in samples "*after cycling in H_2SO_4*".

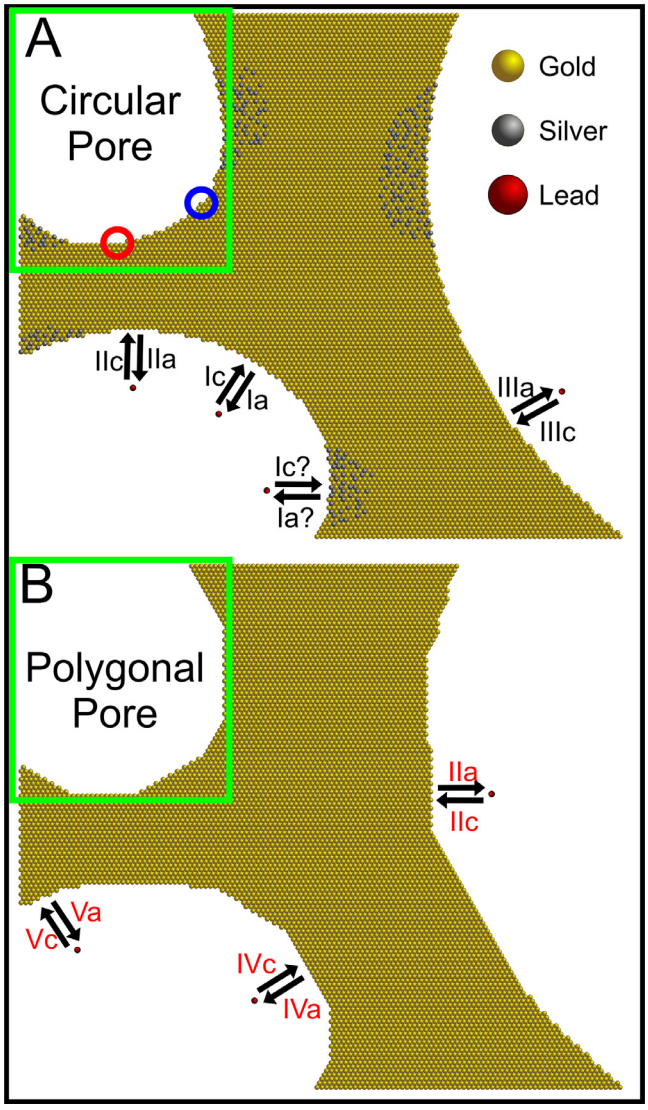

Fig. 4. Sketches representing the geometry of the ligaments in sample (A) *"as prepared"* and (B) *"after cycling in H_2SO_4"*. Circle in red encloses a concave defect and circle in blue encloses a convex defect. Squares in green highlight the variation of the pore geometry.

3.3. Selective partial coverage of the NPG surface by Pb UPD layers

Figure 5 shows the cyclic voltammograms of an NPG sample *"after cycling in H_2SO_4"* at different plumbite ($[Pb(OH)_m]^{(2-m)-}$) concentrations that were obtained by dissolving different amounts of $Pb(NO_3)_2$ in 0.1 M KNO_3 + 0.1 M KOH solution. In addition to being a function of the electrode potential, the Pb UPD coverage also

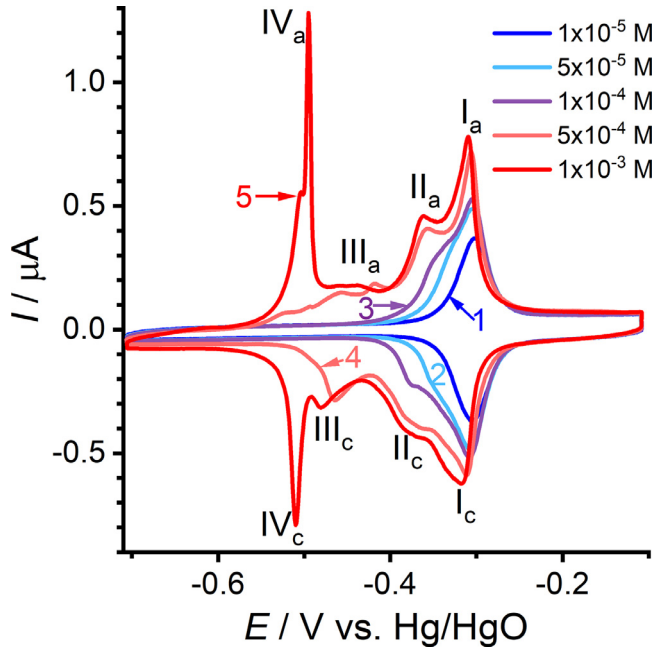

Fig. 5. Comparison of the voltammograms (5th cycle, v = 10 mV s^{-1}) of NPG in the Pb UPD zone *"after cycling in H_2SO_4"*. Background electrolyte was + 0.1 M KNO_3 + 0.1 M KOH with addition of different concentrations of $Pb(NO_3)_2$ (converted to $[Pb(OH)_m]^{(2-m)-}$) (1) 1×10^{-5} M, (2) 5×10^{-5} M, (3) 1×10^{-4} M, (4) 5×10^{-4} M, (5) 1×10^{-3} M.

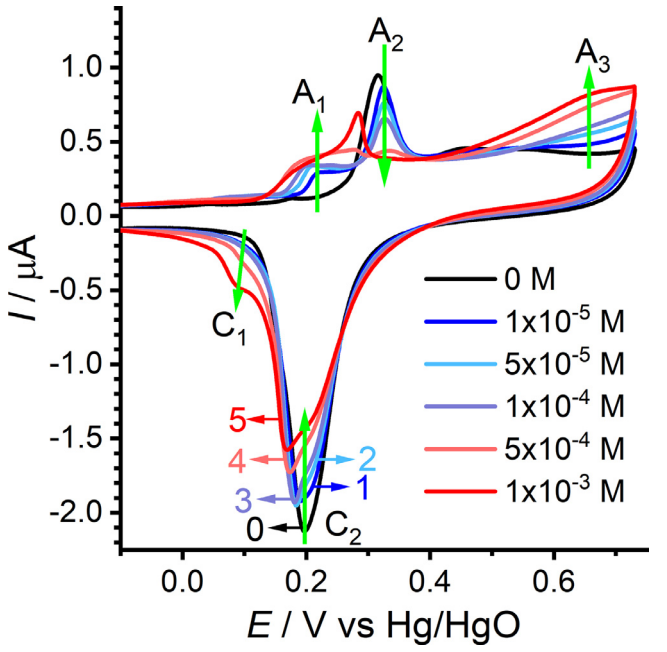

Fig. 6. Comparison of the voltammograms (1st cycle, v = 10 mV s^{-1}) of NPG *"after cycling in H_2SO_4"* in the potential region of gold surface oxidation. Background electrolyte was + 0.1 M KNO_3 + 0.1 M KOH with addition of different concentrations of $Pb(NO_3)_2$ (converted to $[Pb(OH)_m]^{(2-m)-}$) (1) 0, (2) 1×10^{-5} M, (3) 5×10^{-5} M, (4) 1×10^{-4} M, (5) 5×10^{-4} M, (6) 1×10^{-3} M..

depends on the plumbite bulk concentration as the dissolved lead species contained in the pore space of NPG are not sufficient to cover the entire internal surface of NPG. The coverage increases with the plumbite bulk concentration from curves 1 to 5 in Fig. 5. At low plumbite concentration the amount of Pb species is only sufficient to cover the energetically most favorable places (curve 1 Fig. 5) giving rise to the peaks I_c and I_a between -0.39 V and -0.24 V. This remains the only detectable signal even if the potential excursion is made as negative as -0.70 V. After a five-fold increase of the plumbite concentration to 5×10^{-5} M, a shoulder appears at -0.33 V at the position of the peaks II_c/II_a (Fig. 5, curve 2). This trend continues in curve 3, which already shows a clear indication of peak II_c at -0.37 V. The peaks II_c/II_a are almost completely developed in curve 4 (5×10^{-4} M plumbite). In addition, the potential range in which UPD processes occur becomes wider including the potential of peaks III_c/III_a. This suggests that the additional coverage forms on the {110} domains and defects surrounding them. This also explains why peak III_a is not as sharp as observed on single crystal electrodes [47]. This can be associated with a highly stepped surface with slightly varying energies depending on the distance from the nearest step. Finally, curve 5 (1×10^{-3} M plumbite) agrees with the voltammogram in Fig. 3B, in which the entire surface is covered by the lead UPD layer.

The selective partial coverage of the surface of a polycrystalline electrode is an achievement which expands the diagnostic possibilities of UPD processes. The finding is surprising because the solution contains enough Pb species to form a complete monolayer on the small amount of NPG in CME even at the lowest bulk plumbite concentration. However, the supply of Pb for the inner surface area of the porous electrode must come mainly from the pore volume. The typical pore diameter is in the order of 40 nm and thus rapidly depleted from Pb species within the timescale of the experiment. Only the outer surface of the NPG sample within the CME experiences a larger diffusional flux of plumbites by hemispherical diffusion to the microelectrode. The inner parts are less accessible, making the supply of the Pb species from outside the porous network very difficult. As consequence, the system exhibits a mass transport-controlled deposition [62], but with several times higher saturation times due to the hindered mass transport inside the porous structure. This restricted access allows us to selectively decorate the different surface sites in the sequence of their UPD potentials. Overall, the adjustment of the bulk plumbite concentration (by the amount of dissolved $Pb(NO_3)_2$) allows selective blocking of specific surface sites on NPG. This opens the door for exploring the specific catalytic activity of those sites.

Figure 6 shows the voltammogram in the potential region of NPG surface oxidation in alkaline solution at different plumbite concentrations. Dissolved Pb species also affect the surface oxidation of NPG depending on the concentration. Compared to curve 1 (black line), the peaks A_1 and A_3 appear upon addition of $Pb(NO_3)_2$ while the peak A_2 decreases in the positively going scan. Peak A_1 is found at a potential below that of NPG surface oxidation indicating that Pb species are involved in this oxidation. Peak A_2 is the gold surface oxidation and peak A_3 is also related to the presence of Pb species. Peaks A_1 and A_3 increase with increasing bulk plumbite concentration. This result suggests that the oxidation of NPG is hindered by the presence Pb species which are oxidized instead. The statement is confirmed by the decrease of the surface oxide reduction signal C_2 with increasing plumbite concentrations. Concomitantly, the cathodic peak C_1 grows higher with increasing plumbite concentration.

Previous studies have suggested that peaks A_1/C_1 correspond to the oxidation of $[Pb(OH)_m]^{(2-m)-}$ to a thin PbO_2–like oxide layer [48] and peak A_3 corresponds to the bulk growth of the PbO_2 oxide [47]. A reduction peak associated with A_3 is not present because the reduction overlaps with the peak C_2 due to the kinetic control of the process [47,48]. The overlap is evident from the changing shape of signal A_2 in Fig. 6.

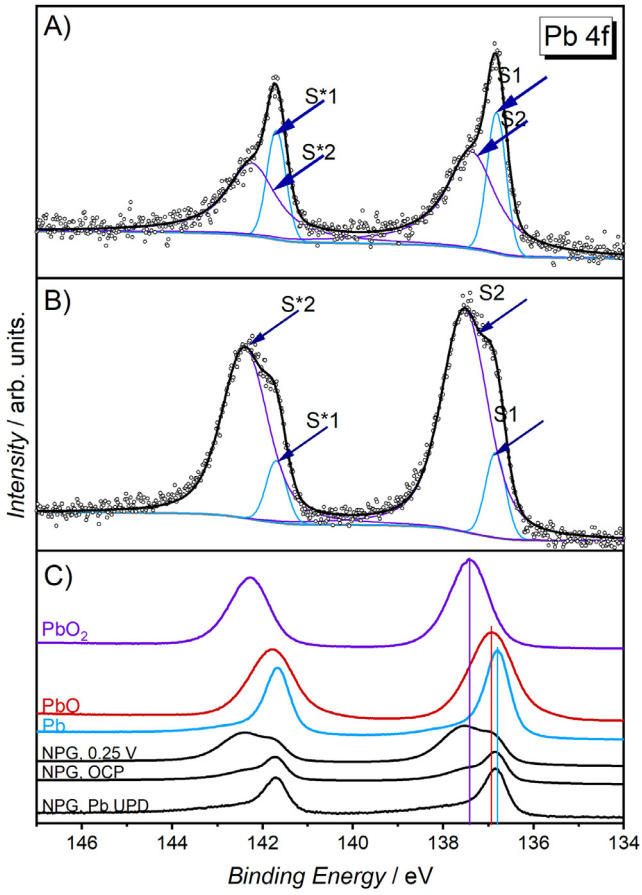

Fig. 7. XPS spectra of NPG *"after cycling in H_2SO_4"* polarized in 1×10^{-3} M plumbate + 0.1 M KNO_3 + 0.1 M KOH (by addition of $Pb(NO_3)_2$); (A) at open circuit potential (-0.320 V vs. Hg/HgO) and (B) at 0.254 V vs. Hg/HgO; (C) Comparison of spectra from PbO_2 powder, PbO powder, Ar^+-sputtered Pb metal as references with NPG emersion from Pb containing KOH at +0.254 V (same as (B), NPG with Pb UPD at OCP (same as A) and NPG with Pb UPD at -0.625 V. Vertical lines in C indicate E_B for the respective Pb $4f_{7/2}$ component of the references.

3.4. Nature of the adsorbed Pb species

On order to confirm the identity of the species involved in these redox processes, high resolution X-ray photoelectron spectroscopy (XPS) was performed on the sample after oxidation of the NPG surface by potential jump in 1×10^{-3} M plumbite + 0.1 M KNO_3 + 0.1 M KOH solution inside a glove box directly attached to the XPS instrument. The sample was then transferred to a carbon tape attached on the sample holder, and then transferred to the XPS ultra-high vacuum system without intermittent contact to oxygen from air. Results are shown in Fig. 7.

Figure 7A shows the result obtained for the sample exposed at open circuit potential (OCP). The deconvolution of the Pb $4f_{7/2}$ doublet shows two signal components S_1 (binding energy E_B = 136.8 eV) and S_2 (E_B = 137.4 eV) [with their Pb $4f_{5/2}$ doublets S^*_1 (E_B = 141.7 eV) and S^*_2 (E_B = 142.2 eV)]. E_B of signal S_1 corresponds to metallic Pb [63] suggesting that the UPD of Pb occurs to some extent spontaneously at OCP. Its value of -0.320 V (obtained after several minutes) lays clearly within the potential range of Pb UPD in Figs. 3B and 5. The signal S_2 can be assigned to an oxidized form of Pb, such as $[Pb(OH)_m]^{(2-m)-}$ anions specifically adsorbed to the NPG surface. The occurrence of multiple oxidation states of Pb on the NPG surface is not a surprising result given that the measured OCP and the voltammograms in Fig. 3B or curve 5 in Fig. 5 show that only a fraction of the surface is covered by metallic UPD Pb at OCP while the other part remains free for the specific adsorption of plumbites present in the solution.

When the sample is polarized at 0.254 V in the same solution before inert transfer to the XPS instrument, signal S_2 (E_B = 137.52 eV) becomes the dominant signal component and shifts slightly to higher E_B (Fig. 7B). The E_B value of this signals agrees with those of Pb_3O_4 ($Pb^{II}_2[Pb^{IV}O_4]$) [64] or PbO_2 [65] that could be formed by dehydration of the hydroxide present in the solution once the sample is placed in the UHV chamber. The components S_1 is shifted by 0.1 eV compared to Fig. 7A, which is within the experimental uncertainty. A comparison to reference spectra in Fig. 7C shows that E_B could agree to PbO and $Pb^{(0)}$. The occurrence of Pb^{II} species is plausible. Considering both, the peak observed in the CV around 0.25 V in Fig. 6 plus the signal S_2 in Fig. 7B, we conclude that at least some lead species are converted to Pb^{IV} at this potential.

3.5. Methanol oxidation reaction at NPG

3.5.1. Effect of the added base

Methanol reacts with the electrolyte in an acid-base equilibrium [Eq. (1)] to form the methoxide anion and water

$$CH_3OH + OH^- \rightleftharpoons CH_3O^- + H_2O. \quad (1)$$

In order to evaluate the effect of the added base and its concentration on MOR, voltammograms of *"as-prepared"* NPG were recorded in 1 M MeOH and a variable concentration of NaOH or KOH (Fig. 8). The voltammograms in NaOH (Fig. 8A) and KOH (Fig. 8B) have the same shape with a feature-less zone between -0.70 and -0.40 V, in which the sample behaves as discussed for Fig. 2. There is a broad oxidation peak I_{a1} between -0.40 V and 0.46 V in the positively going scan, which has been assigned to the oxidation of methanol to formate [66,67]:

$$CH_3OH + 5\ OH^- \rightarrow HCOO^- + 4\ H_2O + 4\ e^- \quad (2)$$

At potential positive of 0.46 V the anodic current increases again (I_{a2}). There are two possible processes at this potential, the further oxidation of formate [Eq. (3)] and the oxidation of methanol directly to carbon dioxide [Eq. (4)] [67]:

$$HCOO^- + 3\ OH^- \rightarrow CO_3^{2-} + 2H_2O + 2e^- \quad (3)$$

$$CH_3OH + 8\ OH^- \rightarrow CO_3^{2-} + 6\ H_2O + 6\ e^- \quad (4)$$

If all formate formed in peak I_{a1} would react further to carbonate according to Eq. (3) the current ratio should be 2:1 based on the number of electrons per substrate molecule. However, peak I_{a2} is clearly larger than that expectations. Therefore, methanol oxidation to carbon dioxide according to Eq. (4) has to take place at this high potential to account for the observed currents. The peaks in KOH are higher than in NaOH, i.e. I_{a1} in KOH > I_{a1} in NaOH and I_{a2} in KOH > I_{a2} in NaOH evidencing a higher catalytic activity of KOH for both processes.

Tafel plots derived from the positively going scan of the cyclic voltammograms, in the potential range between -0.65 V and 0.25 V, are shown in Fig. 8C for NaOH and Fig. 8D for KOH. The equilibrium potential, from which the overpotential η was derived, was calculated from the Gibbs free energy of the half reaction $CH_3OH + H_2O \rightarrow HCOOH+4H^+ + 4e^-$ from tabulated data [68], and converted to Hg/HgO/1 M NaOH reference electrode potential by the equation $E_{Hg/HgO} = E_{SHE} - 0.140$ V, yielding -0.430 V vs. Hg/HgO. Two different linear zones were found summarized in Tables 1 and 2. The first lineal zone appears for η between 0.05 V and 0.1 V with a Tafel slope quoted as $\partial\eta/\partial\log[j/(\text{A cm}^{-2})]$ of 0.1 V/dec for NaOH and KOH solutions. The regions are highlighted

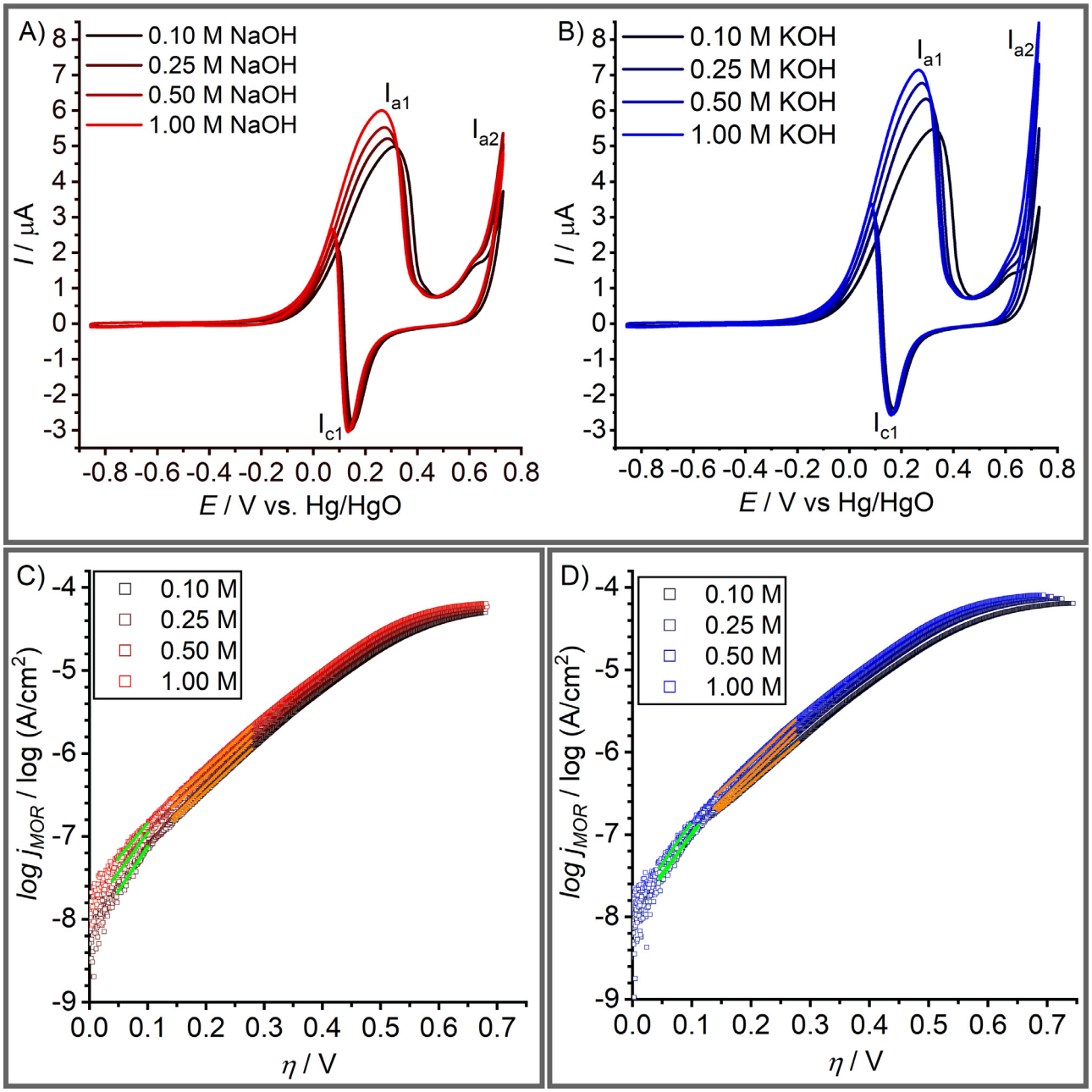

Fig. 8. Voltammogram of "as prepared" NPG sample in (A) 1 M MeOH and different concentrations of NaOH. (B) 1 M MeOH and different concentrations of KOH. (C) Tafel pots for the oxidation of 1 M MeOH at different concentration of NaOH. (D) Tafel pots for the oxidation of 1 M MeOH at different concentration of KOH. Linear zones reported in Tables 1 and 2 are highlighted in green and orange. $v = 10$ mV s^{-1} (For interpretation of the references to color in this figure legend, the reader is referred to the web version of this article.).

by green lines in Fig. 8C and 8D. The Tafel slopes do not change with the base concentration within the investigated concentration range. The same observation is seen in the second linear zone for η between 0.14 and 0.28 V and a Tafel slope $\partial\eta/\partial\log[j/(\mathrm{A\ cm^{-2}})]$ very close to 0.15 V for all electrolytes. The region is highlighted by orange lines in Fig. 8C and 8D. This equality of the behavior in the investigated electrolytes indicates that the rate-determining-step (rds) is neither affected by the concentration nor by the nature of the base.

The exchange current density j_0 was obtained from the intercept of the regression line of the j-η plot or η between 0.05 V and 0.1 V (green lines in Fig. 8C and 8D) and is summarized in Tables 1 and 2. The value of j_0 increases with the concentration of the electrolyte (Tables 1 and 2). On the basis of the generalized Butler-Volmer equation [69], it is possible to relate j_0 to the surface concentration Γ_{act} of active sites and the height of the activation barrier [Eq. (5), [70]]:

$$j_0 = \left(\frac{k_B T n_e \Gamma_{act}}{h}\right) \exp\left(\frac{-G^{\neq}_{rds}}{k_B T}\right) \quad (5)$$

Here k_B is Boltzmann's constant, T is the absolute temperature, n is the number of electrons transferred in the overall reaction, e is the charge of an electron, h is Plank's constant, Γ_{act} is the surface concentration of active sites, and $G^{\#}_{rds}$ is the free enthalpy of the transition state for the rate-determining step (rds). For the peak I_{a1}, four electrons are transferred per methanol molecule as stablished above for the conversion of methanol to formate. At fixed temperature, only Γ_{act} and $G^{\#}_{rds}$ can vary in Eq. (5). For all curves,

Table 1
Summary of parameter stablished form Tafel analysis of MOR at as prepared NPG in NaOH.

Region 1 (0.05 V < η < 0.1 V)					
Conc[M]	Tafel Slope[V/dec]	Intercept[V]	R^2	α	j_o[A cm^{-2}]
0.10	0.095	0.780	0.97084	**0.38**	6.57×10^{-9}
0.25	0.092	0.754	0.91443	**0.36**	6.25×10^{-9}
0.50	0.104	0.823	0.91253	**0.43**	1.21×10^{-8}
1.00	0.118	0.907	0.94545	**0.50**	2.07×10^{-8}
Region 2 (0.14 V < η < 0.28 V)					
Conc[M]	Tafel Slope[V/dec]	Intercept[V]	R^2	α	j_o[A cm^{-2}]
0.10	0.149	1.192	0.99958	**0.61**	1.06×10^{-8}
0.25	0.146	1.129	0.99907	**0.59**	1.76×10^{-8}
0.50	0.154	1.165	0.99939	**0.62**	2.67×10^{-8}
1.00	0.156	1.164	0.99925	**0.62**	3.49×10^{-8}

Table 2
Summary of parameter stablished form Tafel analysis of MOR at *"as prepared"* NPG in KOH.

Region 1 (0.05 V < η < 0.1 V)					
Conc[M]	Tafel Slope[V/dec]	Intercept[V]	R^2	α	j_o[A cm^{-2}]
0.10	0.098	0.788	0.97364	**0.40**	9.69×10^{-9}
0.25	0.107	0.853	0.97817	**0.45**	1.16×10^{-8}
0.50	0.095	0.766	0.94002	**0.38**	9.43×10^{-9}
1.00	0.096	0.756	0.95477	**0.39**	1.31×10^{-8}
Region 2 (0.14 V < η < 0.28 V)					
Conc[M]	Tafel Slope[V/dec]	Intercept[V]	R^2	α	j_o[A cm^{-2}]
0.10	0.162	1.230	0.99965	**0.63**	2.45×10^{-8}
0.25	0.146	1.121	0.99949	**0.60**	2.16×10^{-8}
0.50	0.142	1.086	0.99892	**0.59**	2.29×10^{-8}
1.00	0.147	1.099	0.99916	**0.60**	3.30×10^{-8}

the current rise above the background commences at -0.42 V. For brevity we refer to this potential as "onset potential". The constancy of this value indicates that the energy barrier $G^{\#}_{rds}$ is not affected by the concentration of OH^- in solution. Consequently, the increase of OH^- concentration in solution increases Γ_{act} available to perform the reaction.

The Tafel slopes in zone 1 (green lines) behave differently in NaOH (Fig. 8C) and KOH (Fig. 8D). At low η, the Tafel slopes increase with NaOH concentration evidencing a dependency of the driving force required for MOR on the base concentration. This dependency is broken at higher η (zone 2, orange), where Tafel slopes, and thus symmetry factors, are very similar for all the studied concentrations. Likely the acid-base equilibrium established between methanol and methoxide [Eq. (1)] does not affect the rds at this potential range. In KOH the Tafel slope does not change with concentration in both linear regions suggesting that the rds is not affected by the acid-base equilibrium (1) at all, probably because the reactive species is methoxide.

Kwon et al. [71] have argued that the higher activity of gold for alcohol oxidation in alkaline media is due to the deprotonation of the alcohol to form the reactive alkoxide by reaction (1) in the bulk solution rather than to a surface effect. Because KOH is a slightly stronger base than NaOH, the degree of deprotonation of methanol is higher in KOH than in NaOH solutions, resulting in a higher concentration of the methoxide anion in KOH. Following the argumentation of Kwon et al. [71], there would be a higher methoxide concentration in KOH solution than in NaOH solution at any given added methanol concentration, which increases the reaction rate in KOH and consequently the measured current as it is observed here. This confirms that the deprotonation of the alcohol is a crucial step and these results serve as an additional proof for the active role of the base towards MOR on gold.

3.5.2. Effect of the residual Ag on NPG surface towards MOR

NPG has residual Ag decorating at the surface of ligaments that may play an additional role in MOR at elevated pH. As it was discussed before, the sample *"after cycling in H_2SO_4"* exhibit a lower mole fraction x_{Ag} of residual Ag on the surface of ligaments, which provides a way to compare the effect of residual Ag on MOR. Figure 9A compares the voltammograms obtained for "*as-prepared*" NPG (curve 1, black) and NPG "*after cycling in H_2SO_4*" (curve 2, blue) in 1 M MeOH + 0.25 M KOH. Easily detectable changes in the voltammogram are highlighted by green arrows. The first remarkable difference is the shift of the "onset potential" to more positive values for NPG with lower x_{Ag}. At the same time the currents are lower for potentials negative of the peak I_{a1}, for the sample with x_{Ag} < 1 % indicating an active role of Ag in the first steps of the methanol oxidation. From a magnified image of the voltammograms (not shown) the onset potential was established as -0.36 V for NPG sample "*after cycling in H_2SO_4*" (x_{Ag} < 1%), and as -0.43 V for the *"as prepared"* sample ($x_{Ag} \approx$ 13%). However, the actual peak current $I_{p,a1}$ is higher for NPG with the lower x_{Ag}. Two effects must be considered to rationalize the finding: *i*) lower x_{Ag} means higher x_{Au} available to perform the MOR and *ii*) the sample "*after cycling in H_2SO_4*" has not only a reduced x_{Ag} but also a more faceted surface with wider {111} domains, which are more active (vide supra) for MOR [72] and other alcohols [73] at higher potentials. Peak I_{a2} is several times higher for the sample with higher x_{Ag}, showing a strong catalytic effect for the CO_3^{2-} formation. The reduction peak I_{c1} shows the same features already discussed in connection with Fig. 2.

The Tafel plots in Fig. 9B were calculated from the positively going scan in Fig. 9A between -0.67 V and 0.23 V and show a different behavior of the *"as-prepared"* NPG and NPG *"after cycling in H_2SO_4"*. The *"as-prepared"* NPG shows an initial sluggish reaction

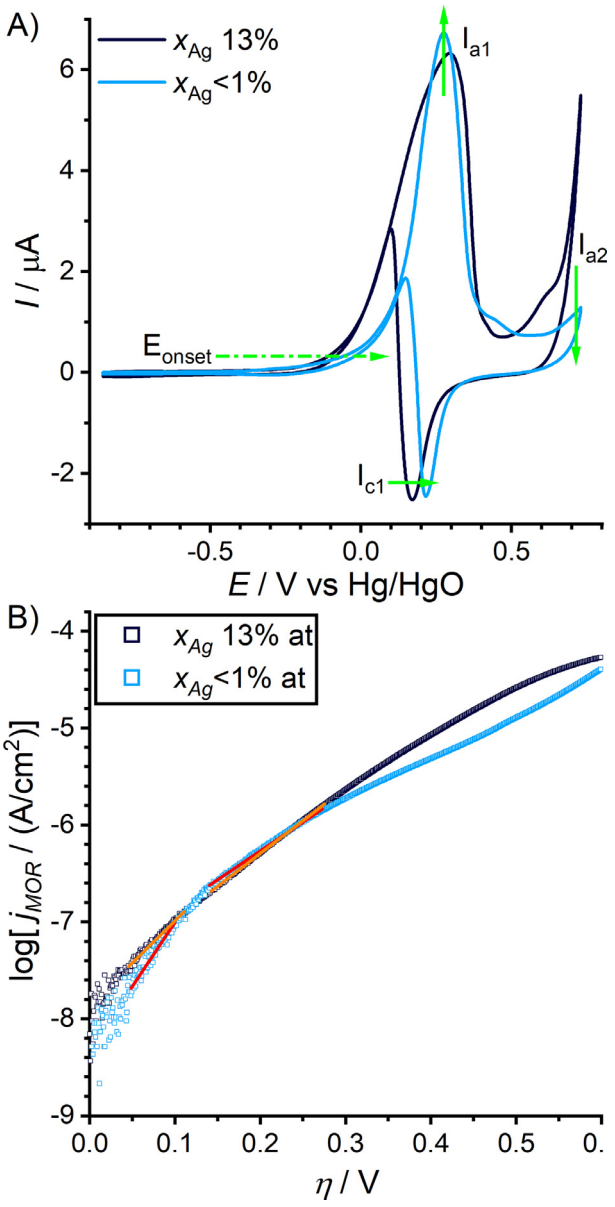

Fig. 9. (A) Voltammogram of *"as-prepapred"* NPG (curve in black) and at NPG *"after cycling in H_2SO_4"* (curve in blue) in 1 M MeOH + 0.25 M KOH. (B) Tafel pots for the oxidation of 1 M MeOH in 0.25 M KOH. Linear zones reported in Table 2 and 2 are highlighted in orange and red; ν = 10 mV s^{-1}. x_{Ag} atomic ratio was obtained from XPS analysis by comparison of the peak area of Au $4f_{7/2}$ and Ag $3d_{5/2}$ (For interpretation of the references to color in this figure legend, the reader is referred to the web version of this article.).

for η between 0.05 V and 0.1 V followed by a wide linear zone or η between 0.15 V and 0.27 V and finally the change to mass-transport control. Values are summarized in Table 3. The curve for NPG *"after cycling in H_2SO_4"* exhibits a clear change of the slope $\partial\eta/\partial\log[j/(\mathrm{A\ cm^{-2}})]$ at 0.14 V. For η > 0.14 V a clearly higher overpotential is needed to increment the logarithm of j. Afterwards, the dependence of the overpotential slightly decrease until mass-transport control commences.

We assume that the first step of the reaction is the oxidative adsorption of the methoxide [Eq. (6)] followed by the removal of H_β either by solution OH^- [Eq. (8)] or adsorbed $(OH)^*$ [Eq. (9)]. Here * denotes adsorbed intermediates:

$$H_\beta CH_2O^- \rightarrow (H_\beta CH_2O)^* + e^- \quad (6)$$

$$H_3COH + (OH)^* \rightarrow (H_3CO)^* + H_2O \quad (7)$$

$$(H_\beta CH_2O)^* + OH^- \rightarrow (CH_2O)^* + HOH_\beta + e^- \quad (8)$$

$$(H_\beta CH_2O)^* + (OH)^* \rightarrow (CH_2O)^* + HOH_\beta + e^- \quad (9)$$

This result of the Tafel analysis suggests that the rds is the first electron transfer (ET) [Eq. (6)] at the *"as-prepared"* NPG with a high x_{Ag}, whereas it is the second ET [Eqs. (8) or (9)] at NPG *"after cycling in H_2SO_4"*, at which x_{Ag} is low.

When assuming that the first step of the reaction is the oxidative adsorption of the methoxide [Eq. (6)] followed by the removal of the H_β by solution or adsorbed OH^- [Eqs. (8) and (9)], Ag promotes the oxidative adsorption and thus lowers the onset potential required to trigger the reaction. Residual Ag may also facilitate the adsorption of OH^- on the surface,

$$OH^- + * \rightarrow (OH)^* + e^- \quad (10)$$

or provide the oxygen necessary for the partial oxidation of the surface required to promote the oxidative adsorption of methanol [Eq. (7)] as it has been shown in previous reports [66,67,71,72,74]. This hypothesis is also supported by a previous report [49], where it was demonstrated that Ag remains at the surface mainly as Ag^I species during the methanol oxidation on NPG and that the elemental distribution of Ag is dynamic within the ligaments, i.e. Ag can segregate from the inner part of the ligaments to the surface and change its oxidation state there.

3.5.3. Effect of adsorbed Pb species on the NPG surface towards MOR

Figure 10A shows the MOR voltammograms of NPG *"after cycling in H_2SO_4"* in 1 M MeOH + 0.5 M KOH + 0.1 M KNO_3 with the addition of variable concentration of $Pb(NO_3)_2$ (converted to plumbites). All experiments started at -0.657 V applied for 120 s before initiating the potential scan. It is expected that the maximum possible surface coverage is reached for this potential and plumbite bulk concentration. The potential region highlighted in the black rectangle in Fig. 10A shows the Pb UPD signals that were already discussed in detail in connection with Fig. 5. The increase of plumbite bulk concentration causes an increase of the surface concentration of Pb species as evidenced by the rising UPD signals. In the region of MOR at potentials positive of -0.1 V, the MOR current rise shifts to more positive potentials with increasing plumbite concentration. This behavior shows a competition for the adsorption sites of the NPG between methanol and plumbite anions, that changes completely the MOR on the NPG surface. However, close to 0.05 V the systems with the two lowest plumbite coverages (curves 2 and 3 in Fig. 10A) show *higher* current densities than the Pb-free system (curve 1), indicating a higher catalytic effect for MOR than bare NPG. This trend persists up to the peak potential at 0.3 V, where the highest peak current is measured for the system with 5×10^{-5} M plumbite bulk concentration (curve 3 in Fig. 10A).

Very interesting is the positively going scan in curve 4 of Fig. 10A for a plumbite bulk concentration of 1×10^{-4} M. Similar to the curves discussed before, the "onset potential" is shifted to more positive potentials. However, this is followed by two potential regions (0.05 V to 0.18 V, and 0.23 V to 0.4 V), in which the currents are higher than in the Pb-free solution. This different behavior in different potential regions is necessarily connected to different slopes ($\partial I/\partial E$), which are directly related to the electrocatalytic activity of the adsorbed Pb species on the NPG surface in different potential regions, which will be discussed below by means of Tafel plots. Finally, curves 5 and 6 show a dramatic decay of the peak currents. The UPD zone shows that {111} domains of NPG are increasingly covered when the plumbite bulk concentration rises

Table 3
Summary of parameter stablished form Tafel analysis of MOR in KOH for sample *"after cycling in H_2SO_4"*.

Region 1 (0.05 V < η < 0.1 V)					
Conc[M]	Tafel Slope[V/dec]	Intercept[V]	R^2	α	j_o[A cm^{-2}]
0.10	0.089	0.744	0.96146	**0.34**	4.56×10^{-9}
0.25	0.076	0.631	0.92456	**0.22**	4.77×10^{-9}
Region 2 (0.20 V < η < 0.28 V)					
Conc[M]	Tafel Slope[V/dec]	Intercept[V]	R^2	α	j_o[A cm^{-2}]
0.10	0.182	1.364	0.99804	**0.68**	3.21×10^{-8}
0.25	0.179	1.319	0.99777	**0.67**	4.26×10^{-8}

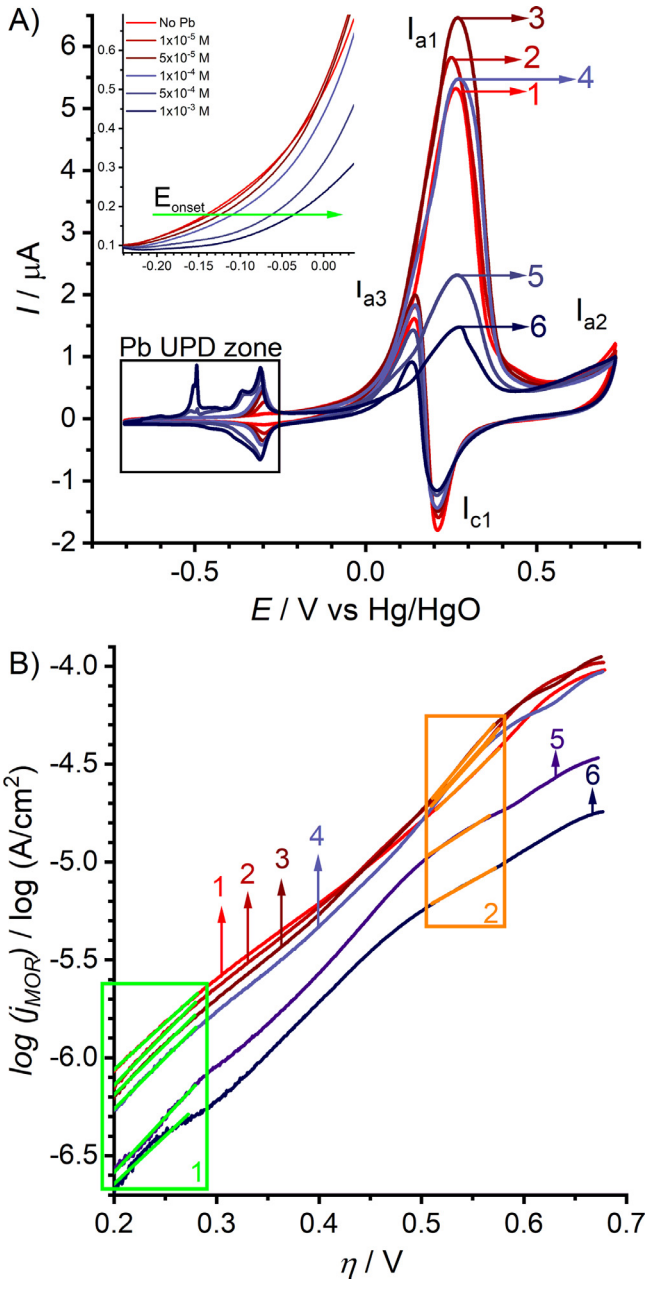

Fig. 10. (A) Comparison of the voltammograms of *"after cycling in H_2SO_4"* NPG in 1 M MeOH + 0.1 M KNO_3 + 0.1 M KOH and a variable amount of $Pb(NO_3)_2$ (converted to $[Pb(OH)_m]^{(2-m)+}$) (1) 0, (2) 1×10^{-5} M, (3) 5×10^{-5} M, (4) 1×10^{-4} M, (5) 5×10^{-4} M, (6) 1×10^{-3} M; ν = 10 mV s^{-1}. (B) Tafel plots between the end of the UPD zone and the peak I_a.

from 1×10^{-4} M (curve 4) to 1×10^{-3} M (curve 6). Compared to the variation of MOR current in curves 2–4, the decrease of MOR activity cannot be explained by a proportionally higher coverage of the surface by Pb species that block the Au sites. Contrary to expectations from chemically activated Au electrodes [75], the defects which provide the UPD site of high potential do not contribute the largest fraction to the catalytic MOR oxidation current. Instead, they seem to be important for the OH^- adsorption. The catalytic MOR current at NPG only drops substantially if the plumbite bulk concentration is high enough so that the wide {111} domains are covered in the UPD process. This finding mirrors MOR results from Au single crystals electrodes [67], in which the highest activity was found for the (111) surface.

Tafel plots were constructed from the positively going scans of the CVs in Fig. 10A and are depicted in Fig. 10B. In order to facilitate the analysis, only two potential regions with an overpotential η < 0.3 V and 0.45V < η < 0.55 V will be considered in detail. The zone η < 0.3 V shows the influence of the competition between methoxide, OH^- and Pb species for surface sites on the first reaction steps. An increasing plumbite bulk concentration shifts the Tafel lines to more negative log[j/(A cm^{-2})] values and increases the Tafel slope $\partial\eta/\partial\log[j/(\text{A cm}^{-2})]$ suggesting that the surface concentration of active sites concomitantly increases with the energetic barrier because Pb species displace $(CH_3O)^*$ from the surface. However, $(CH_3O)^*$ is required for the reaction in Eqs. (8) and (9). At low plumbate concentration, only $(OH)^*$ adsorbed on the defects and {110} domains are blocked. At the same time, the "onset potential" shifts to more positive values, proving that a higher driving force is required for the MOR. In agreement with Beyhan et al. [73], the {110} domains are the more reactive surface at low overpotential. The inhibition becomes extreme when even the {111} domains are covered by Pb species as depicted by curves 5 and 6 in Fig. 10A and the strong shift to lower values on the log[j/(A cm^{-2})] values and high Tafel slope value of those curves in Fig. 10B.

At higher overpotential the behavior becomes complicated, but between 0.45 V and 0.55 V, it is clear that Tafel slope for curves 2 – 4 is lower than for curve 1, indicating that those systems require less driving force (overpotential) to increase the current, which is a clear signal of the catalytical effect. This suggests that the Pb species adsorbed on the NPG surface become catalytical for MOR providing even better conditions than the $(OH)^*$ on NPG. This means, that curves 2–4 have a lower Tafel slope $\partial\eta/\partial\log[j/(\text{A cm}^{-2})]$ compared to curve 1. That is an important observation not only to understand the reactivity of the NPG surface towards MOR, but also to unveil the role of external metals decorating the surface, such as Pb or Ag and their corresponding alkaline anionic species. In this case, we suppose a non-oxidative adsorption of the Pb anions at low overpotential followed by a partial oxidation of those species at more positive potentials. For Pb the following reaction may lead to

$$[Pb(OH)_m]^{(2-m)-} + * \rightarrow [Pb(OH)_m]^{(2-m)-}{}_{ads} \quad (11)$$

$$[Pb(OH)_m]^{(2-m)-}{}_{ads} \rightarrow [Pb(OH)_m]^{(4-m)-}{}_{ads} + 2e^- \quad (12)$$

$[Pb(OH)_m]^{(4-m)-}{}_{ads}$ may release water to form PbO_2 or react with Pb^{II} species to form Pb_3O_4. The oxidation state of +4 for the product in Eq. (12) is supported by the XPS analysis in Fig. 7A, where Pb_3O_4 or PbO_2 was found. This species, as well as Ag oxides discussed in a previous section, seem to play ta similar role as defects on gold surfaces, which are partially oxidized when OH^- adsorbs, providing the surface conditions to facilitate the first step of MOR. Interestingly, the catalytic activity is only observable at low coverages, this is when only defects and {110} facets are covered. This suggests that the first step takes place on the defects and {110} facets, while the further steps occur on {111} facets, where the stabilization of the intermediates is more effective than on other structures making up the ligament surface. This hypothesis is also supported by the abrupt decay of the peak current I_{a1} in the curve 5 compared to curve 4 of Fig. 10A. This change occurs exactly upon the increase of the Pb solution concentration that causes UPD also on the {111} facets. The conclusion on the role of low index planes is further supported by the comparison between the peaks I_{a1} for MOR at *"as-prepapred"* NPG and NPG *"after cycling in H_2SO_4"* in Fig. 9A. When Ag is removed from the surface by cycling in H_2SO_4, the surface rephases forming wider {111} facets (as discussed in Section 2.2) and thus leading to a larger peak current (highlighted with the arrow in green).

Beyond the peak potential of I_{a1} in Fig. 10A, the surface oxidizes and the reaction (3) and (4) are not promoted by PbO_2 deposited on NPG. This is different to the behavior observed on the "*as prepared*" samples with residual Ag on the surface. Instead, the behavior shown at potentials positive of 0.50 V fits more to a bulk growth of the PbO_2 layer than to CO_3^{2-} production. This fact is a direct evidence of the requirement of a thin oxide layer of gold to promote the transfer of 6 electrons, which is covered by the bulk growth of PbO_2. This statement is confirmed by the behavior of peak I_{a3}, which is the reactivation of the surface towards MOR once the oxidized NPG surface has been reduced, showing a similar trend as I_{a1}.

4. Conclusions

The surface structure of nanoporous gold is stabilized by residual Ag that segregates to the surface after the dealloying procedure. Residual Ag can be dissolved by short potential cycling in H_2SO_4. The removal of Ag triggers the restructuring of the ligament surface from a curved, defect-rich one with narrow terraces to a more stable faceted surface with wider low index terraces. This can be demonstrated by Pb UPD experiments with NPG in a cavity microelectrode. The high internal surface area of NPG enables the selective partial blockage of different sites on the NPG surface by adjustment of the plumbite bulk concentration. First, defect near {110} domains are occupied, followed by the {110} domains themselves, and lastly the {111} domains and some defects near the flat {111} and {110} domains at high plumbite concentrations. To the best of our knowledge, this is the first time that this behavior is purposefully used for UPD experiments. Together with the removal of surface segregated Ag, selective Pb UPD can subsequently be used to disentangle the influence of different surface features of this polycrystalline material on electrocatalytic reactions.

As an example, the as prepared and rephased NPG samples show different activity towards methanol oxidation in alkaline solutions. In the presence of residual Ag on the as prepared surfaces, the MOR commences at lower potentials. It also promotes the six-electron oxidation to CO_2/CO_3^{2-} at the oxide-covered surface (high positive potential). However, the maximum current is smaller than on rephased NPG, illustrating the role of {110} and {111} terraces for the electrocatalysis. This evidence is further supported by selective blockage of those sites by Pb UPD or plumbite adsorption after which the current drops substantially. A detailed Tafel analysis shows that the {110} terraces are more reactive structures at low overpotential probably by promotion of the oxidative adsorption of hydroxide anions. However, when those sites are occupied by Pb UPD or plumbites, the peak current does not decrease as much as when the {111} facets are blocked, showing that in fact the most active structures for MOR are the {111} domains and the defects are important for the first step of the reaction.

Independently on the presence of residual Ag, the catalytic effect increases with higher base concentration for NaOH and KOH. At equal concentration, KOH yields higher currents. The analysis of Tafel plots shows that the exchange current density j_0 and the energetic barrier to reach the transition state $G^{\#}_{rds}$ are equally affected in both electrolytes, proving that the alkaline media not only enhance the surface conditions for the electrocatalysis of MOR, but also has a chemical catalytic effect by deprotonating the methanol molecule to form methoxide in an acid-base equilibrium. As such, the stronger base KOH is more effective.

Interestingly, Pb species adsorbed on the surface at *low coverages* also show an electrocatalytic effect which is reminiscent to the effect of residual Ag. At low overpotentials the oxidation current commences at lower potentials. The mechanism can be similar to reactions occurring on "*as prepared*" samples with residual Ag at the surface that causes high concentration of $(OH)^*$. Pb species also promote the six-electron oxidation at higher potential when voltammetry and XPS analysis indicates the presence of Pb^{IV} species at the ligament surface. However, at higher plumbite bulk concentration, the formation of CO_2 is inhibited, probably due to the growth of a thicker PbO_2 layer that covers the NPG surface.

Declaration of Competing Interest

The authors declare that they have no known competing financial interests or personal relationships that could have appeared to influence the work reported in this paper.

Acknowledgments

The support of Deutsche Forschungsgemeinschaft is gratefully acknowledge for funding the Research Group FOR2213-255613253 [subprojects 3 and 4] as well as for partial funding of the central facilities of the School of Mathematics and Science for SEM (INST 184/107-1 FUGG) and XPS instrumentation (INST 184/144-1 FUGG).

References

[1] K. Hu, D. Lan, X. Li, S. Zhang, Electrochemical DNA biosensor based on nanoporous gold electrode and multifunctional encoded DNA-Au bio bar codes, Anal. Chem. 80 (2008) 9124–9130.
[2] Z. Liu, J. Du, C. Qiu, L. Huang, H. Ma, D. Shen, Y. Ding, Electrochemical sensor for detection of p-nitrophenol based on nanoporous gold, Electrochem. Commun. 11 (2009) 1365–1368.
[3] Z. Matharu, P. Daggumati, L. Wang, T.S. Dorofeeva, Z. Li, E. Seker, Nanoporous-gold-based electrode morphology libraries for investigating structure-property relationships in nucleic acid based electrochemical biosensors, ACS Appl. Mater. Interfaces 9 (2017) 12959–12966, doi:10.1021/acsami.6b15212.
[4] X.Y. Lang, H.T. Yuan, Y. Iwasa, M.W. Chen, Three-dimensional nanoporous gold for electrochemical supercapacitors, Scr. Mater. 64 (2011) 923–926, doi:10.1016/j.scriptamat.2011.01.038.
[5] X. Lang, L. Zhang, T. Fujita, Y. Ding, M. Chen, Three-dimensional bicontinuous nanoporous Au/polyaniline hybrid films for high-performance electrochemical supercapacitors, J. Power Sources 197 (2012) 325–329.
[6] J. Biener, A. Wittstock, L.A. Zepeda-Ruiz, M.M. Biener, V. Zielasek, D. Kramer, R.N. Viswanath, J. Weissmüller, M. Bäumer, A.V. Hamza, Surface-chemistry-driven actuation in nanoporous gold, Nat. Mater. 8 (2009) 47–51, doi:10.1038/nmat2335.
[7] H.-J. Jin, X.-L. Wang, S. Parida, K. Wang, M. Seo, J. Weissmüller, Nanoporous Au-Pt alloys as large strain electrochemical actuators, Nano Lett. 10 (2010) 187–194.

[8] C. Yu, F. Jia, Z. Ai, L. Zhang, Direct oxidation of methanol on self-supported nanoporous gold film electrodes with high catalytic activity and stability, Chem. Mater. 19 (2007) 6065–6067.

[9] J. Zhang, P. Liu, H. Ma, Y. Ding, Nanostructured porous gold for methanol electro-oxidation, J. Phys. Chem. C 111 (2007) 10382–10388.

[10] A. Wittstock, A. Wichmann, M. Bäumer, Nanoporous gold as a platform for a building block catalyst, ACS Catal. 2 (2012) 2199–2215.

[11] A. Wittstock, V. Zielasek, J. Biener, C.M. Friend, M. Bäumer, Nanoporous gold catalysts for selective gas-phase oxidative coupling of methanol at low temperature, Science 327 (2010) 319–322, doi:10.1126/science.1183591.

[12] A. Lackmann, C. Mahr, M. Schowalter, L. Fitzek, J. Weissmüller, A. Rosenauer, A. Wittstock, A comparative study of alcohol oxidation over nanoporous gold in gas and liquid phase, J. Catal. 353 (2017) 99–106, doi:10.1016/j.jcat.2017.07.008.

[13] Y. Ding, J. Erlebacher, Nanoporous metals with controlled multimodal pore size distribution, J. Am. Chem. Soc. 125 (2003) 7772–7773, doi:10.1021/ja035318g.

[14] Z. Wang, S. Ning, P. Liu, Y. Ding, A. Hirata, T. Fujita, M. Chen, Tuning surface structure of 3D nanoporous gold by surfactant-free electrochemical potential cycling, Adv. Mater. 29 (1703601) (2017) 1–7 /, doi:10.1002/adma.201703601.

[15] Y. Ding, M. Chen, J. Erlebacher, Metallic mesoporous nanocomposites for electrocatalysis, J. Am. Chem. Soc. 126 (2004) 6876–6877, doi:10.1021/ja0320119.

[16] A. Lackmann, M. Bäumer, G. Wittstock, A. Wittstock, Independent control over residual silver content of nanoporous gold by galvanodynamically controlled dealloying, Nanoscale 10 (2018) 17166–17173, doi:10.1039/c8nr03699c.

[17] S. Reculusa, M. Heim, F. Gao, N. Mano, S. Ravaine, A. Kuhn, Design of catalytically active cylindrical and macroporous gold microelectrodes, Adv. Funct. Mater. 21 (2011) 691–698, doi:10.1002/adfm.201001761.

[18] E. Seker, L.M. Reed, R.M. Begley, Nanoporous gold, Materials (2009) 2188–2215.

[19] A. Wittstock, J. Biener, M. Bäumer, Introduction to nanoporous gold, RSC Nanosci. Nanotechnol. 22 (2012) 1–10.

[20] R.C. Newman, S.G. Corcoran, J. Erlebacher, M.J. Aziz, K. Sieradzki, Alloy corrosion, MRS Bull. 24 (1999) 24–28, doi:10.1557/S0883769400052660.

[21] H. Okamoto, T.B. Massalski, The Ag–Au (Silver-Gold) system, Bull. Alloy Phase Diagrams 4 (1983) 30–38, doi:10.1007/BF02880317.

[22] R. Morrish, K. Dorame, A.J. Muscat, Formation of nanoporous Au by dealloying AuCu thin films in HNO_3, Scr. Mater. 64 (2011) 856–859.

[23] Q. Zhang, X. Wang, Z. Qi, Y. Wang, Z. Zhang, A benign route to fabricate nanoporous gold through electrochemical dealloying of Al-Au alloys in a neutral solution, Electrochim. Acta 54 (2009) 6190–6198.

[24] Z. Zhang, Y. Wang, Y. Wang, X. Wang, Z. Qi, H. Ji, C. Zhao, Formation of ultrafine nanoporous gold related to surface diffusion of gold adatoms during dealloying of Al2Au in an alkaline solution, Scr. Mater. 62 (2009) 137–140, doi:10.1016/j.scriptamat.2009.10.018.

[25] G.-F. Han, B.-B. Xiao, X.-Y. Lang, Z. Wen, Y.-F. Zhu, M. Zhao, J.-C. Li, Q. Jiang, Self-Grown $Ni(OH)_2$ layer on bimodal nanoporous AuNi alloys for enhanced electrocatalytic activity and stability, ACS Appl. Mater. Interfaces 6 (2014) 16966–16973, doi:10.1021/am504541a.

[26] J.-F. Huang, I.-W. Sun, Fabrication and surface functionalization of nanoporous gold by electrochemical alloying/dealloying of Au-Zn in an ionic liquid, and the self-assembly of L-Cysteine monolayers, Adv. Funct. Mater. 15 (2005) 989–994.

[27] J. Erlebacher, An atomistic description of dealloying, J. Electrochem. Soc. 151 (2004) C614–C626, doi:10.1149/1.1784820.

[28] Z. Zhang, Y. Wang, Z. Qi, W. Zhang, J. Qin, J. Frenzel, Generalized fabrication of nanoporous metals (Au, Pd, Pt, Ag, and Cu) through chemical dealloying, J. Phys. Chem. C 113 (2009) 12629–12636, doi:10.1021/jp811445a.

[29] H.W. Pickering, C. Wagner, Electrolytic dissolution of binary alloys containing a noble metal, J. Electrochem. Soc. 114 (1967) 698–706, doi:10.1149/1.2426709.

[30] H.W. Pickering, Characteristic features of alloy polarization curves, Corros. Sci. 23 (1983) 1107–1120.

[31] M. Graf, B. Roschning, J. Weissmüller, Nanoporous gold by alloy corrosion, J. Electrochem. Soc. 164 (2017) C194–C200, doi:10.1149/2.1681704jes.

[32] C. Mahr, P. Kundu, A. Lackmann, D. Zanaga, K. Thiel, M. Schowalter, M. Schwan, S. Bals, A. Wittstock, A. Rosenauer, Quantitative determination of residual silver distribution in nanoporous gold and its influence on structure and catalytic performance, J. Catal. 352 (2017) 52–58, doi:10.1016/j.jcat.2017.05.002.

[33] L. Zhang, L. Chen, H. Liu, Y. Hou, A. Hirata, T. Fujita, M. Chen, Effect of residual silver on surface-enhanced Raman scattering of dealloyed nanoporous gold, J. Phys. Chem. C 115 (2011) 19583–19587, doi:10.1021/jp205892n.

[34] A. Wittstock, B. Neumann, A. Schaefer, K. Dumbuya, C. Kuebel, M.M. Biener, V. Zielasek, H.-P. Steinrueck, J.M. Gottfried, J. Biener, A. Hamza, M. Bäumer, Nanoporous Au, J. Phys. Chem. C 113 (2009) 5593–5600, doi:10.1021/jp808185v.

[35] T. Krekeler, A.V. Straßer, M. Graf, K. Wang, C. Hartig, M. Ritter, J. Weissmüller, Silver-rich clusters in nanoporous gold, Mater. Res. Lett. 5 (2017) 314–321.

[36] N. Mameka, K. Wang, J. Markmann, E.T. Lilleodden, J. Weissmüller, Nanoporous gold—testing macro-scale samples to probe small-scale mechanical behavior, Mater. Res. Lett. 4 (2016) 27–36, doi:10.1080/21663831.2015.1094679.

[37] L.-Z. Liu, X.-L. Ye, H.-J. Jin, Interpreting anomalous low-strength and low-stiffness of nanoporous gold: quantification of network connectivity, Acta Mater 118 (2016) 77–87, doi:10.1016/j.actamat.2016.07.033.

[38] S. Hoppe, S. Müller, A first principles study on the electronic origins of silver segregation at the Ag-Au (111) surface, J. Appl. Phys. 122 (235303) (2017) 1–9 /, doi:10.1063/1.5017959.

[39] T. Fujita, P. Guan, K. McKenna, X. Lang, A. Hirata, L. Zhang, T. Tokunaga, S. Arai, Y. Yamamoto, N. Tanaka, Y. Ishikawa, N. Asao, Y. Yamamoto, J. Erlebacher, M. Chen, Atomic origins of the high catalytic activity of nanoporous gold, Nat. Mater. 11 (2012) 775–780, doi:10.1038/nmat3391.

[40] T. Fujita, T. Tokunaga, L. Zhang, D. Li, L. Chen, S. Arai, Y. Yamamoto, A. Hirata, N. Tanaka, Y. Ding, M. Chen, Atomic observation of catalysis-induced nanopore coarsening of nanoporous gold, Nano Lett. 14 (2014) 1172–1177, doi:10.1021/nl403895s.

[41] S. Hoppe, Y. Li, L.V. Moskaleva, S. Mueller, How silver segregation stabilizes 1D surface gold oxide, Phys. Chem. Chem. Phys. 19 (2017) 14845–14853, doi:10.1039/C7CP02221B.

[42] M. Haensch, M. Graf, W. Wang, A. Nefedov, C. Wöll, J. Weissmüller, G. Wittstock, Thermally driven Ag–Au compositional changes at the ligament surface in nanoporous gold: implications for electrocatalytic applications, ACS Appl. Nano Mater. 3 (2020) 2197–2206, doi:10.1021/acsanm.9b02279.

[43] A.R. Silva Olaya, B. Zandersons, G. Wittstock, Restructuring of nanoporous gold surface during electrochemical cycling in acidic and alkaline media, ChemElectroChem 7 (2020) 3670–3678, doi:10.1002/celc.202000923.

[44] J. Snyder, P. Asanithi, A.B. Dalton, J. Erlebacher, Stabilized nanoporous metals by dealloying ternary alloy precursors, Adv. Mater. 20 (2008) 4883–4886, doi:10.1002/adma.200702760.

[45] A. Hamelin, Underpotential deposition of lead on single crystal faces of gold, J. Electroanal. Chem. (1984) 167–180.

[46] A. Hamelin, J. Lipkowski, Underpotential Deposition of lead on gold single crystal faces, J. Electroanal. Chem. 171 (1984) 317–330.

[47] J. Hernandez, J. Solla-Gullón, E. Herrero, Gold nanoparticles synthesized in a water-in-oil microemulsion, J. Electroanal. Chem. 574 (2004) 185–196.

[48] R.R. Adžić, A.V. Tripković, N.M. Marković, Oxygen reduction on electrode surfaces modified by foreign metal ad-atoms: lead ad-atoms on gold, J. Electroanal. Chem. 114 (1980) 37–51.

[49] M. Graf, M. Haensch, J. Carstens, G. Wittstock, J. Weissmüller, Electrocatalytic methanol oxidation with nanoporous gold, Nanoscale 9 (2017) 17839, doi:10.1039/c7nr05124g.

[50] M.L. Tremblay, M.H. Martin, C. Lebouin, A. Lasia, D. Guay, Determination of the real surface area of powdered materials in cavity microelectrodes by electrochemical impedance spectroscopy, Electrochim. Acta 55 (2010) 6283–6291, doi:10.1016/j.electacta.2009.11.006.

[51] N. Mameka, J. Markmann, H.-J. Jin, J. Weissmüller, Electrical stiffness modulation—confirming the impact of surface excess elasticity on the mechanics of nanomaterials, Acta Mater. 76 (2014) 272–280, doi:10.1016/j.actamat.2014.04.067.

[52] N. Mameka, J. Markmann, J. Weissmüller, On the impact of capillarity for strength at the nanoscale, Nat. Commun. 8 (2017) 1976, doi:10.1038/s41467-017-01434-2.

[53] L. Lührs, B. Zandersons, N. Huber, J. Weissmüller, Plastic Poisson's ratio of nanoporous metals: a macroscopic signature of tension-compression asymmetry at the nanoscale, Nano Lett. 17 (2017) 6258–6266, doi:10.1021/acs.nanolett.7b02950.

[54] A. Hamelin, M.J. Sottomayor, F. Silva, S.-C. Chang, M.J. Weaver, Cyclic voltammetric characterization of oriented monocrystalline gold surfaces in aqueous alkaline solution, J. Electroanal. Chem. 295 (1990) 291–300.

[55] A. Hamelin, A. Katayama, G. Picq, P. Vennereau, Surface characterization by underpotential deposition, J. Electroanal. Chem. Interfac. Electrochem. 113 (1980) 293–300.

[56] J. Hernandez, J. Solla-Gullon, E. Herrero, J.M. Feliu, A. Aldaz, In situ surface characterization and oxygen reduction reaction on shape-controlled gold nanoparticles, J. Nanosci. Nanotechnol. 9 (2009) 2256–2273, doi:10.1166/jnn.2009.SE38.

[57] J. Hernandez, J. Solla-Gullón, E. Herrero, A. Aldaz, J.M. Feliu, Characterization of the surface structure of gold nanoparticles and nanorods using structure sensitive reactions, J. Phys. Chem. B 109 (2005) 12651–12654, doi:10.1021/jp0521609.

[58] A. Bewick, B. Thomas, Optical and electrochemical studies of the underpotential deposition of metals, J. Electroanal. Chem. 84 (1977) 127–140.

[59] R. Adzic, E. Yeager, B.D. Cahan, Optical and electrochemical studies of underpotential deposition of lead on gold evaporated and single-crystal electrodes, J. Electrochem. Sci. Technol. 121 (1974) 474–484.

[60] L. Yu, R. Akolkar, Lead underpotential deposition for the surface characterization of silver ad-atom modified gold electrocatalysts for glucose oxidation, J. Electroanal. Chem. 792 (2017) 61–65, doi:10.1016/j.jelechem.2017.03.037.

[61] V. Grasmik, C. Rurainsky, K. Loza, M.V. Evers, O. Prymak, M. Heggen, K. Tschulik, M. Epple, Deciphering the surface composition and the internal structure of alloyed silver-gold nanoparticles, Chem. Eur. J. 24 (2018) 9051–9060, doi:10.1002/chem.201800579.

[62] E. Kirowa-Eisner, Y. Bonfil, D. Tzur, E. Gileadi, Thermodynamics and kinetics of UPD of lead on polycrystalline silver and gold, J. Electroanal. Chem. 552 (2003) 171–183, doi:10.1016/s0022-0728(03)00181-5.

[63] S. Rondon, P.M.A. Sherwood, Core level and valence band spectra of lead by XPS, Surf. Sci. Spectra 5 (1998) 83–89, doi:10.1116/1.1247864.

[64] S. Rondon, P.M.A. Sherwood, Core level and valence band spectra of Pb_3O_4 by XPS, Surf. Sci. Spectra 5 (1998) 90–96, doi:10.1116/1.1247865.

[65] S. Rondon, P.M.A. Sherwood, Core level and valence band spectra of PbO_2 by XPS, Surf. Sci. Spectra 5 (1998) 104–110, doi:10.1116/1.1247867.

[66] K.A. Assiongbon, D. Roy, Electro-oxidation of methanol on gold in alkaline media: Adsorption characteristics of reaction intermediates studied using time resolved electro-chemical impedance and surface plasmon resonance techniques, Surf. Sci. 594 (2005) 99–119, doi:10.1016/j.susc.2005.07.015.

[67] Z. Borkowska, A. Tymosiak-Zielinska, G. Shul, Electrooxidation of methanol on polycrystalline and single crystal gold electrodes, Electrochim. Acta 49 (2004) 1209–1220, doi:10.1016/j.electacta.2003.09.046.
[68] W.M. Haynes, D.R. Lide, CRC Handbook of Chemistry and Physics: A Ready-reference Book of Chemical and Physical Data, CRS Press, Boca Raton, 2014.
[69] R. Parsons, General equations for the kinetics of electrode processes, Trans. Faraday Soc. 47 (1951) 1332–1344.
[70] K.S. Exner, I. Sohrabnejad-Eskan, H. Over, A universal approach to determine the free energy diagram of an electrocatalytic reaction, ACS Catal. 8 (2018) 1864–1879, doi:10.1021/acscatal.7b03142.
[71] Y. Kwon, S.C.S. Lai, P. Rodriguez, M.T.M. Koper, Electrocatalytic oxidation of alcohols on gold in alkaline media: base or gold catalysis? J. Am. Chem. Soc. 133 (2011) 6914–6917, doi:10.1021/ja200976j.
[72] P. Rodriguez, M.T.M. Koper, Electrocatalysis on gold, Phys. Chem. Chem. Phys. 16 (2014) 13583–13594, doi:10.1039/c4cp00394b.
[73] S. Beyhan, K. Uosaki, J.M. Feliu, E. Herrero, Electrochemical and in situ FTIR studies of ethanol adsorption and oxidation on gold single crystal electrodes in alkaline media, J. Electroanal. Chem. 707 (2013) 89–94, doi:10.1016/j.jelechem.2013.08.034.
[74] P. Rodriguez, Y. Kwon, M.T.M. Koper, The promoting effect of adsorbed carbon monoxide on the oxidation of alcohols on a gold catalyst, Nat. Chem. 4 (2011) 177–182, doi:10.1038/nchem.1221.
[75] Z. Borkowska, A. Tymosiak-Zielinska, R. Nowakowski, High catalytic activity of chemically activated gold electrodes towards electro-oxidation of methanol, Electrochim. Acta 49 (2004) 2613–2621, doi:10.1016/j.electacta.2004.01.030.